

**UCLA**

**UCLA Electronic Theses and Dissertations**

**Title**

Evaluating Reactions in Exhausts of Deposition Reactors for Safe Semiconductor Manufacturing

**Permalink**

<https://escholarship.org/uc/item/45b6d56j>

**Author**

Park, Dong-Sung Brian

**Publication Date**

2024

Peer reviewed|Thesis/dissertation

UNIVERSITY OF CALIFORNIA

Los Angeles

Evaluating Reactions in Exhausts of Deposition Reactors for Safe Semiconductor  
Manufacturing

A dissertation submitted in partial satisfaction of the  
requirements for the degree Master of Science  
in Chemical Engineering

by

Dong-Sung Brian Park

2024

© Copyright by

Dong-Sung Brian Park

2024

## ABSTRACT OF THE DISSERTATION

Evaluating Reactions in Exhausts of Deposition Reactors for Safe Semiconductor

Manufacturing

by

Dong-Sung Brian Park

Master of Science in Chemical Engineering

University of California, Los Angeles 2024

Professor Jane Pei-Chen Chang, Chair

In semiconductor manufacturing, safety concerns regarding the use of highly reactive precursors, which are volatile and pyrophoric by nature, arise from potential energetic reactions in the downstream exhaust lines of deposition reactors. Mishaps have been reported in the recent decade when an excess of unreacted precursors or pyrophoric byproducts reacts among themselves or with other gases. In order to reduce risks and develop a mitigating strategy for a safe working environment, it is imperative to have a comprehensive understanding through monitoring of the reactions, formation, and accumulation of hazardous compounds in the utilized tools.

This study evaluates silane chemistry for plasma-enhanced chemical vapor deposition (PECVD) and trimethyl aluminum and tetrakis (dimethyl amido) hafnium chemistries for atomic layer deposition (ALD) using *in-situ* and *ex-situ* Fourier transform infrared (FTIR) and X-ray photoelectron spectroscopy (XPS) techniques to support safety measures during semiconductor processing.

In the PECVD downstream exhaust line, the use of silane, nitrous oxide, and ammonia

resulted in an averaged mass accumulation of 0.15 mg per hour of silane at a flow rate of 20 sccm. The FTIR analysis indicated O-H and Si-OH stretching vibrational nodes, and their signals intensified with the accumulated deposits. Combining with the Si-O bonds observed by XPS analysis, the formation of silanol, which is unstable, flammable, and toxic, is indicated.

In the ALD downstream exhaust line, the use of trimethyl aluminum, tetrakis (dimethyl amido) hafnium, and water resulted in an averaged mass accumulation of 0.20 mg per hour of hafnium precursor gas with a 0.25 second pulse per cycle at 20 sccm. The FTIR analysis was unable to distinguish absorbance peaks of Al-OH and Hf-OH contributing to metallic hydroxide. However, the observed deposition is unlikely from aluminum precursor, based on XPS analysis, which showed the atomic composition of hafnium hydroxide and oxide increased with increasing processing time, but Al 2p features were not observed. Since metal hydroxides have highly exothermic reactions with low flash points and auto ignition temperatures, byproducts can act as unforeseen ignition sources, and their formation should be minimized.

This study emphasizes the inherent safety problems in semiconductor fabrication, particularly those associated with the use of volatile and pyrophoric precursors in deposition reactors. A buildup of unstable, flammable, and toxic silanol was observed in the PECVD system, while metal hydroxides with exothermic properties formed in the downstream of the ALD tool. This monitoring result established insight into understanding compositions in the exhaust line, enabling prospects for designing ways to reduce safety hazards and provide a safe working environment.

The dissertation of Dong-Sung Brian Park is approved.

Samanvaya Srivastava

Dante Simonetti

Jane Pei-Chen Chang, Committee Chair

University of California, Los Angeles

2024

## TABLE OF CONTENTS

CHAPTER 1: INTRODUCTION .....	1
1.1 Motivation .....	1
1.2 Prediction of Energetic Reactions in Exhaust of Processing Systems .....	5
1.3 Chemicals of Concern Related to Energetic Reactions .....	7
1.4 Infrared Absorbance Studies of Thin Film Deposits .....	11
1.5 Scope and Organization .....	15
CHAPTER 2: EXPERIMENTAL SETUP .....	17
2.1 Exhaust Monitoring Deposition Chambers .....	17
2.1.1 Plasma-Enhanced Chemical Vapor Deposition Chamber .....	17
2.1.2 Atomic Layer Deposition Chamber .....	18
2.1.3 Monitoring System .....	20
2.1.4 Potassium Bromide Pellet .....	21
2.2 Material Characterization Techniques .....	24
2.2.1 Fourier Transform Infrared Spectroscopy .....	24
2.2.2 X-ray Photoelectron Spectroscopy .....	27
2.3 Summary .....	29
CHAPTER 3: MONITORING AND ANALYSIS OF PECVD SYSTEM .....	31
3.1 Growth Experiment in PECVD Chamber .....	32
3.2 <i>In-situ</i> Fourier Transform Infrared Experiment .....	34
3.3 Exhaust Monitoring Experiment .....	35
3.4 Summary .....	41
CHAPTER 4: MONITORING AND ANALYSIS OF ALD SYSTEM .....	43
4.1 Growth Experiment in ALD Chamber .....	44
4.2 Exhaust Monitoring Experiment .....	46
4.3 Summary .....	50
CHAPTER 5: SUMMARY .....	53
Appendix .....	56
Bibliography .....	76

## LIST OF FIGURES

- Figure 1.1 The number of energetic events between 2010 and 2013 were caused by 3 materials outside the tool, 11 materials supplied to the tool, 7 materials inside the tool, 47 downstream of the tool, and 4 waste materials (Trammel, 2014). .....3
- Figure 1.2 (a) Disilane precursor hazard resulting in two-inch steel exhaust bellows and Klein Flansche (KF) clamps destroyed (adapted from Westmoreland, 2011). (b) Schematic diagram of deposition tool downstream line represented in Equations 1.5 - 1.7. During the exhaust gas flow to process tool to treatment, the reactive species R may lead to formation of deposition and ultimately local hotspot given the right conditions (Watson, 2020). .....4
- Figure 1.3 (a) Silane reaction pathway from pyrolysis, different ratio reaction with H<sub>2</sub>O, and reaction with H<sub>3</sub>SiOH (adapted Liu, 2022). (b) Calculated Gibb's free energy with silane that are exothermic reactions and potentially contribute to forming hazardous compounds (HSC and Liu, 2021).....9
- Figure 1.4 (a) Trimethyl aluminum (TMA) reaction pathway from pyrolysis, different reactions with O and O<sub>2</sub>. (adapted from Liu, 2022). (b) Calculated Gibb's free energy with TMA that are exothermic reactions and potentially contribute to forming hazardous compounds (HSC & Liu, 2021). ..... 10
- Figure 1.5 (a) Absorption spectra of SiO<sub>2</sub> with varying time using Fourier transform infrared (FTIR) spectroscopy. The plasma-enhanced chemical vapor deposition was kept at RF power of 100 W, substrate temperature of 250 °C, 25 mTorr, and gas flowrate of 50 sccm (adapted from Han, 1996). (b) Absorption spectra of Al<sub>2</sub>O<sub>3</sub> FTIR absorbance scans with different cycles of 0.5 s trimethyl aluminum (TMA)/H<sub>2</sub>O atomic layer deposition at 103°C (adapted from Sperling, 2020)...... 14
- Figure 2.1 (a) A schematic diagram of a plasma-enhanced chemical vapor deposition (PECVD) tool used in this work, with *in-situ* Fourier transform infrared (FTIR) spectroscopy implemented in the exhaust for monitoring. (b) A top view illustration of the *in-situ* FTIR chamber for in-line monitoring of the PECVD thin film deposition process in the exhaust line (adapted from Cho, 2015). ..... 18
- Figure 2.2 A schematic diagram of an atomic layer deposition (ALD) tool used in this work. .... 19
- Figure 2.3 (a) A schematic diagram of experimental setup with the KBr locations indicated. Currently, only plasma-enhanced chemical vapor deposition has implemented an *in-situ* Fourier transform infrared setup, while the atomic layer deposition exhaust line is interconnected with three other tools. (b) The adaptor tee schematic attached exhaust lines to with stainless steel mesh pellets to place KBr pellets in the downstream lines.....21



Figure 2.4 (a) 13mm pellet die set schematic with (1) die base, (2) die body, (3) die pellets, (4) plunger, and (5) sample holder (adapted from Chemplex ®, 2019). To create an infrared transparent pellet, place 140 mg KBr powder (5) and assemble the die set before applying 10,000 lb with hydraulic press (Appendix 3). (b) Variation of twelve as-made KBr pellet masses and their corresponding initial KBr powder masses.....22

Figure 2.5 (a) Absorbance infrared spectra of twelve KBr pellets as references for post-deposition analysis. (b) The thin film deposition features from as-taken data of 7 hours of SiH<sub>4</sub>, 5 hours of N<sub>2</sub>O, and 2 hours of NH<sub>3</sub> in plasma-enhanced chemical vapor deposition exhaust was subtracted with reference KBr spectrum presented in the bottom spectrum of (a). This processed data was rescaled by 3 times and signals attribute to just IR traces of thin film deposits. ....26

Figure 2.6 (a) A XPS survey spectrum obtained from SiO<sub>2</sub> deposition on a KBr pellet inside the plasma-enhanced chemical vapor deposition reactor. (b) A survey XPS spectrum obtained from Al<sub>2</sub>O<sub>3</sub> on a KBr pellet inside the atomic layer deposition reactor.....28

Figure 3.1 (a) Fourier transform infrared absorbance scans of 1 μm SiO<sub>2</sub> and SiN<sub>x</sub> thin film on KBr pellets deposited in the plasma-enhanced chemical vapor deposition reactor. Scans went through signal averaging and KBr background scan subtraction. High-resolution X-ray photoelectron spectroscopy spectra of (b) O 1s and (c) N 1s regions with atomic percent composition labeled. ....33

Figure 3.2 (a) Fourier transform infrared (FTIR) absorbance scan of multilayer growth experiment using sequential deposition using SiO<sub>2</sub> and SiN<sub>x</sub> on a KBr pellet. (b) *In-situ* FTIR absorbance scan obtained simultaneously during the multilayer growth. Each layer has signal subtracted from the previous scanned layer to represent the topmost deposits. ....35

Figure 3.3 (a) Absolute deposition versus pellet ID (bottom x-axis) and silane exposure time (top x-axis) of plasma-enhanced chemical vapor deposition exhaust extracted pellets. Each extracted pellet was subtracted with its original KBr pellet to show only deposition mass. (b) Process logbook tabulated with processing time and precursors. For SiO<sub>2</sub>, SiN<sub>x</sub>, and chemical cleaning, SiH<sub>4</sub>/N<sub>2</sub>O, SiH<sub>4</sub>/NH<sub>3</sub>, and SF<sub>6</sub>/N<sub>2</sub>O ratios were processed, respectively.....36

Figure 3.4 (a) Absorbance scans of plasma-enhanced chemical vapor deposition exhaust extracted pellets. All spectra are averaged using five different areas of a pellet and subtracted from the KBr background signals. Extracted pellets were exposed to hours of SiH<sub>4</sub>, N<sub>2</sub>O, NH<sub>3</sub>, and SF<sub>6</sub>: (i) 7, 5, 2, 0, (ii) 13, 6, 7, 9, and (iii) 17, 7, 10, 11, and (iv) 3, 2, 1, 4. (Ref) As prepared KBr pellet was scanned for reference. (b) Trend of integrated absorbance intensity of Si-O bending ~1100 at cm<sup>-1</sup>, Si-N bending ~870 at cm<sup>-1</sup>, O-H stretching ~3701 at cm<sup>-1</sup>, and Si-OH stretching at ~3652 cm<sup>-1</sup> regions of each pellet. ....37

Figure 3.5 X-ray photoelectron spectroscopy survey scans of plasma-enhanced chemical vapor deposition exhaust extracted pellets. Extracted pellets were exposed to (i) 0.5 hour of SiH<sub>4</sub>/NH<sub>3</sub>,

(ii) 3 hours of SF<sub>6</sub>, (iii) 1.5 hours of SiH<sub>4</sub>/N<sub>2</sub>O, and (iv) 2 hours of SF<sub>6</sub> prior to extraction. (Ref) As prepared KBr pellet was scanned for reference.....38

Figure 3.6 High-resolution X-ray photoelectron spectroscopy spectra of (a) F 1s, (b) O 1s, (c) K 2p, (d) C 1s, (e) S 2p, (f) Si 2p, and (g) Br 3d regions of extracted pellets from PECVD exhaust. Extracted pellets were exposed to (i) 0.5 hour of SiH<sub>4</sub>/NH<sub>3</sub>, (ii) 3 hours of SF<sub>6</sub>, (iii) 1.5 hours of SiH<sub>4</sub>/N<sub>2</sub>O, and (iv) 2 hours of SF<sub>6</sub> prior to extraction. (Ref) As prepared KBr pellet was scanned for reference. Atomic compositions and possible compounds associated with the binding energy peak are labeled. ....39

Figure 3.7 Pellet ID versus atomic composition graphs of selected electronegative elements. Atomic compositional trends are shown for (a) F 1s, (b) O 1s, (c) S 2p, and (d) Br 3d. Top x-axis is extracted pellets that were exposed to (i) 0.5 hour of SiH<sub>4</sub>/NH<sub>3</sub>, (ii) 3 hours of SF<sub>6</sub>, (iii) 1.5 hours of SiH<sub>4</sub>/N<sub>2</sub>O, and (iv) 2.0 hours of SF<sub>6</sub> prior to extraction. (Ref) As prepared KBr pellet was scanned for reference. The bottom x-axis pellet ID associated with the element atomic composition.....40

Figure 4.1 (a) Fourier transform infrared (FTIR) absorbance scans of 100 cycles growth of Al<sub>2</sub>O<sub>3</sub> and (ii) HfO<sub>2</sub> in atomic layer deposition chamber on KBr pellets. Scans went through signal averaging and KBr background scan subtraction. High-resolution X-ray photoelectron spectroscopy spectra of (b) Al 2p and (c) Hf 4f regions with atomic percent composition are labeled. ....45

Figure 4.2 (a) Absolute deposition versus pellet ID (bottom x-axis) and silane exposure time (top x-axis) of atomic layer deposition exhaust extracted pellets. Each extracted pellet was subtracted with its original KBr pellet to show only deposition mass. (b) Process logbook tabulated with process time and organometallic precursors. For Al<sub>2</sub>O<sub>3</sub> and HfO<sub>2</sub>, Al(CH<sub>3</sub>)<sub>3</sub>/H<sub>2</sub>O and Hf(NMe<sub>2</sub>)<sub>4</sub>/H<sub>2</sub>O cycles were processed, respectively.....46

Figure 4.3 (a) Absorbance scans of atomic layer deposition exhaust extracted pellets. All spectra are averaged using five different areas of a pellet and subtracted from the KBr background signals. Extracted pellets were exposed to hours of Al(CH<sub>3</sub>)<sub>3</sub>, Hf(NMe<sub>2</sub>)<sub>4</sub>, and H<sub>2</sub>O: (i) 12, 2, 14, (ii) 118, 6, 124, (iii) 127, 8, 135, and (iv) 4, 2, 6. (Ref) As prepared KBr pellet was scanned for reference. (b) Trend of integrated absorbance intensity of M-O bending at 800-710 cm<sup>-1</sup>, O-H stretching at ~3700 cm<sup>-1</sup>, M-OH stretching at 3800 – 3650 cm<sup>-1</sup> of each pellet. ....47

Figure 4.4 X-ray photoelectron spectroscopy survey scans of atomic layer deposition exhaust extracted pellets. Extracted pellets were exposed to (i) 3 hours of Hf(NMe<sub>2</sub>)<sub>4</sub>/H<sub>2</sub>O, (ii) 3 hours of Al(CH<sub>3</sub>)<sub>3</sub>/H<sub>2</sub>O, (iii) 0.5 hours of Al(CH<sub>3</sub>)<sub>3</sub>/H<sub>2</sub>O, and (iv) 2 hours of Hf(NMe<sub>2</sub>)<sub>4</sub>/H<sub>2</sub>O prior to extraction. (Ref) As prepared KBr pellet was scanned for reference. ....48

Figure 4.5 High-resolution X-ray photoelectron spectroscopy spectra of (a) F 1s, (b) O 1s, (c) K 2p, (d) C 1s, (e) Br 3d, and (f) Hf 4f regions of extracted pellets from atomic layer deposition

exhaust. Extracted pellets were exposed (i) 3 hours of  $\text{Hf}(\text{NMe}_2)_4/\text{H}_2\text{O}$ , (ii) 3 hours of  $\text{Al}(\text{CH}_3)_3/\text{H}_2\text{O}$ , (iii) 0.5 hours of  $\text{Al}(\text{CH}_3)_3/\text{H}_2$ , and (iv) 2 hours of  $\text{Hf}(\text{NMe}_2)_4/\text{H}_2\text{O}$  prior to extraction. (Ref) As prepared KBr pellet was scanned for reference. Atomic compositions and possible compounds associated with the binding energy peak are labeled. ....49

Figure 4.6 Pellet type versus atomic composition graphs of selected elements. Atomic compositional trends are shown for (a) F1s, (b) O1s, (c) Hf 4f, and (d) Br 3d. Top x-axis is extracted pellets that were exposed to (i) 3 hours of  $\text{Hf}(\text{NMe}_2)_4/\text{H}_2\text{O}$ , (ii) 3 hours of  $\text{Al}(\text{CH}_3)_3/\text{H}_2\text{O}$ , (iii) 0.5 hours of  $\text{Al}(\text{CH}_3)_3/\text{H}_2\text{O}$ , and (iv) 2 hours of  $\text{Hf}(\text{NMe}_2)_4/\text{H}_2\text{O}$  prior to extraction. (Ref) As prepared KBr pellet was scanned for reference. The bottom x-axis is types of pellets associated with the composition.....50

## LIST OF TABLES

Table 1.1 Precursor properties and their safety information (based on reported material safety data sheets).....	8
Table 1.2 Energetic species and their possible product between 25 – 100°C in exhaust lines (Liu, 2022). Compounds H <sub>2</sub> (g), H <sub>2</sub> O (l), H <sub>2</sub> O (g), O (g), O <sub>2</sub> (g), C (s), CO (g), and CO <sub>2</sub> (g) are found in all products of energetic species.....	11
Table 1.3 Literature reported vibrational wavenumbers of surface species involving Si, Al, Hf, O, N, C, and H. ....	15
Table 2.1 Precursors used in the plasma-enhanced chemical vapor deposition system and their properties as listed in the material safety data sheet (MSDS). ....	18
Table 2.2 Precursors used in the atomic layer deposition (ALD) system and their properties as listed in the material safety data sheet (MSDS).....	20
Table 2.3 The pellet ID naming scheme used in this work, where (i), (ii), (iii) stands for pellets extracted from the exhaust lines in a sequential order, typically one month apart, and (Ref) is each corresponding as-prepared KBr pellet. For each sample, the exposure time to the precursors and the last process before extraction are also listed. ....	23
Table 2.4 Different specification of Nexus Thermo Nicolet Fourier transform infrared (FTIR) spectroscopies that were used. <i>In-situ</i> 670 FTIR has custom built chamber and is attached to the exhaust of plasma-enhanced chemical vapor deposition reactor. <i>Ex-situ</i> 8700 FTIR uses KBr beams splitter, MCT detector, and IR source to simulate conditions of <i>in-situ</i> FTIR. ....	25
Table 2.5 Relative sensitivity factor (RSF) values of elements used in X-ray photoelectron spectroscopy (XPS) measurement. (Biesinger, 2021). ....	29

## ACKNOWLEDGEMENTS

I am deeply thankful to generous funding provided by the Semiconductor Research Corporation and the research opportunities from Liaisons, which has played a pivotal role in the successful execution of this research endeavor. Their assistance has not only made it possible to obtain necessary resources, but it has also made a substantial contribution to the growth of knowledge in this area.

I am indebted to Professor Jane Chang for her unmatched counsel and mentoring. Her knowledge, astute criticism, and resolute assistance have been crucial in determining the course of this study and improving its general caliber. Throughout this journey, Professor Chang's dedication to academic excellence has served as a consistent source of inspiration.

I also want to thank my lab mates for their teamwork and collaborative attitude. In the laboratory, a vibrant intellectual environment has been fostered and the research process has been strengthened by the exchange of ideas, varied viewpoints, and teamwork.

Lastly, I would extend heartfelt thanks to my family for their consistent support, understanding, and encouragement over the years. Their support and belief in my academic goals have motivated me, and I am appreciative of their stability and affection, which have made my academic path both worthwhile and satisfying.

## CHAPTER 1: INTRODUCTION

The semiconductor manufacturing industry has undergone changes in response to environmental, health, and safety concerns with the operating reactive precursors that have inherent hazardous properties. The increase in widely used energetic precursor chemistries such as silane and trimethyl aluminum inevitably presents challenges in the exhaust manifolds where control is lacking and condensates and/or fire hazards can accumulate. As long as the industry continues to utilize these potentially hazardous chemicals due to their effectiveness, continuous awareness of risk management needs considering. While effort exists to implement temperature regulation and/or a point-of-use abatement in the exhaust line of each process tool, a direct chemical monitoring and feedback system has not been reported. Therefore, this work aims to aid the safety endeavor by identifying the byproduct formation in the exhaust lines of plasma-enhanced chemical vapor deposition and atomic layer deposition tools.

### 1.1 Motivation

Over the past few decades, the semiconductor industry has undergone exponential technological advancements. These advancements include the creation of integrated circuits, microprocessors, and breakthroughs in nanotechnology, as well as the development of state-of-the-art extreme ultraviolet (UV) lithography for fabricating features as small as 3-5 nm. Despite the benefits of this production, major chemical resources utilized in the industry are hazardous to the environment, health, and safety (EHS). These chemical resources include reproductive toxins, carcinogens, mutagens, and corrosive chemicals in high concentration and purity. When consumed globally in excessive amounts, safety concerns in the industry become of utmost priority. While this consumption cannot be eliminated, different methods of control can be implemented, including engineering, administrative, and personal controls. Since the

value of human life cannot be measured economically, it is vital to prioritize EHS concerns in the semiconductor industry. The semiconductor industry heavily relies on precursors, which account for more than 50% of the chemical resources used. In total, an annual average of 10,495 tons of chemicals are used across  $130 \pm 76$  products (Chambers, 2016). This amounts to a global market revenue of \$610.15 billion USD in 2022 amongst companies like Samsung, Intel, and TSMC and continues to have a significant impact on the global economy (Alda, 2023).

However, the use of chemicals does not always end up in positive results for the industry. Many incidents have been reported while developing intricate chemistries in semiconductor manufacturing. Many of which have energetic properties that can exhibit contamination, leakage, fire, explosions, and chemical reactions. An industrial benchmark conducted by SEMATECH, which has been published as the SEMI S30-1023 safety guideline (SEMI, 2020), shows 72 energetic related accidents resulting in facility and personnel damage. Specifically, handling pyrophoric organometallics like trimethyl aluminum (TMA) resulted in a fire and the creation of submicron aluminum carbide soot. (Trammel, 2014). These energetic events occurred mostly frequently at the downstream of the tool, where a total of 47 incidents were caused by 5 leaks, 23 fires, 9 explosions, and 10 chemical reactions (Figure 1.1). In the downstream sections of tools, byproduct formation and accumulation have been considered culprits for frequent energetic events (Chang, 2019), due to localized deposition buildup.

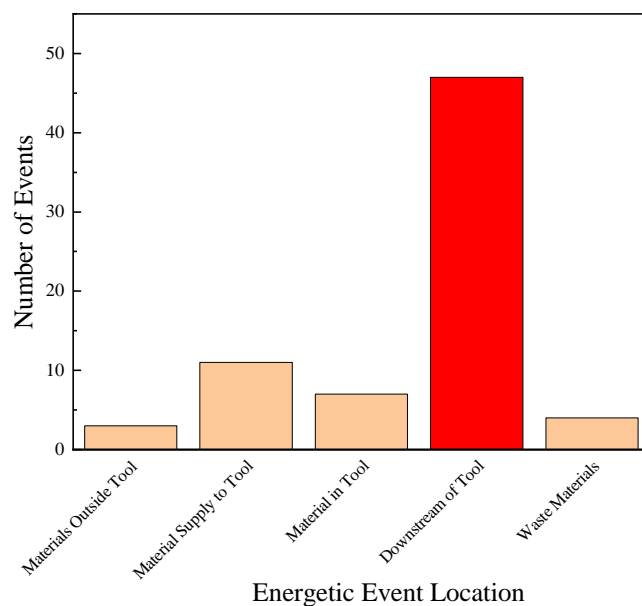


Figure 1.1 The number of energetic events between 2010 and 2013 were caused by 3 materials outside the tool, 11 materials supplied to the tool, 7 materials inside the tool, 47 downstream of the tool, and 4 waste materials (Trammel, 2014).

Accidents involving precursors result in environmental damage, financial impact, legal liabilities, or even the casualties of workers. For example, one TMA accident in the chemical supplier of the semiconductor industry occurred in North Andover, Massachusetts, in 2015. A worker at the Dow Chemical facility was exposed to TMA vapors while conducting maintenance on a reactor vessel. The worker suffered chemical burns and was transported to a hospital for treatment. An investigation by the Occupational Safety and Health Administration (OSHA) found that Dow Chemical had failed to properly label the TMA container and had not provided adequate personal protective equipment to the worker. OSHA also found that Dow Chemical had not conducted a thorough hazard assessment of the maintenance work being performed. As a result of the investigation, Dow Chemical was cited for several safety violations and fined \$126,000. The company was also required to make changes to its safety procedures and provide additional training to its employees (Matthews, 2017). Another silane explosion occurred at the Mitsubishi Materials chemical plant in Yokkaichi, Mie in 2014. The heat exchanger was cleaned with water without knowledge or inspection when it was covered



with highly water reactive trichlorosilane. The resulting catastrophe had a 440-pound reactor lid blown 10 meters away, five deceased, and 12 others injured (Tsuda, 2014). One disilane event happened when the two-inch steel bellows pipe exploded owing to pressure building and a temperature rise caused by byproduct deposits accumulating inside the exhaust (Figure 1.2 (a)). Such damage is not only tragic and costly but can also take years to clean up, along with long-term effects on the ecosystem and human health. The downstream of a deposition tool can be represented as a schematic diagram of Figure 1.2 (b) along with Equations 1.5 – 1.7.

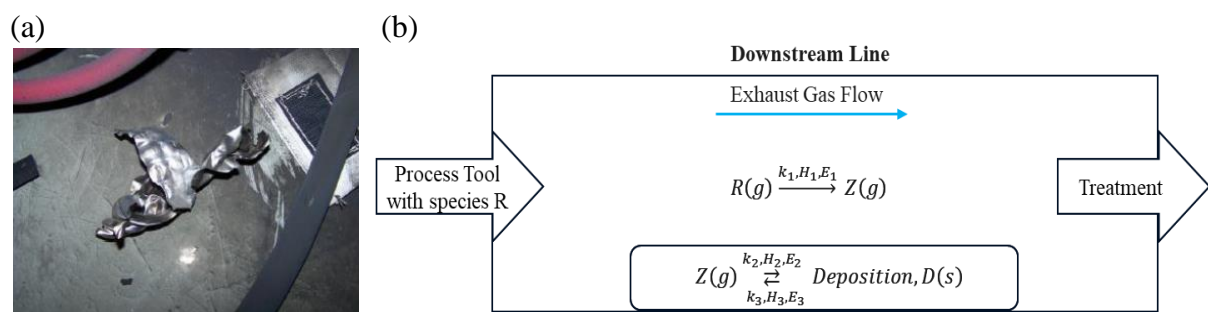


Figure 1.2 (a) Disilane precursor hazard resulting in two-inch steel exhaust bellows and Klein Flansche (KF) clamps destroyed (adapted from Westmoreland, 2011). (b) Schematic diagram of deposition tool downstream line represented in Equations 1.5 - 1.7. During the exhaust gas flow to process tool to treatment, the reactive species R may lead to formation of deposition and ultimately local hotspot given the right conditions (Watson, 2020).

This study aims to focus on the area that lacks control during the manufacturing of integrated circuits. In the exhaust of deposition tools, solid, liquid, and gaseous precursors could interact in unexpected ways. These precursors are prone to forming potentially hazardous byproducts that accumulate on the surfaces of the exhaust line and cause potentially energetic reactions. While most equipment has cleaning procedures to remove deposition from the chamber surfaces, the exhaust lines do not have the same conditions to make the cleaning effective. Consequently, the buildup of deposits could result in local hotspots in the exhaust, where unforeseen energetic reactions have higher tendencies to occur.

## 1.2 Prediction of Energetic Reactions in Exhaust of Processing Systems

The main contribution of deposition formation and buildup in the downstream line occurs where the process conditions in the reactors no longer hold. Thermodynamic assessment can be done to predict the favored products that occur in the downstream area. Utilizing Gibbs free energy minimization, byproducts of various chemical precursors can be identified. Given constant temperature and pressure, the thermal equilibrium can be described as Equation 1.1:

$$G(P, T, \{n_i\}^N) = \sum_{i=1}^N \mu_i n_i (P, T, \{n_i\}) \quad (1.1)$$

where  $G$  is Gibbs free energy,  $P$  is pressure,  $T$  is temperature, species  $i$  have number of moles  $n_i$  and chemical potential  $\mu_i$  in  $N$  number of species. The chemical potential can be further described as Equation 1.2:

$$\mu_i = G_{f,i}(T) + RT \ln \left( \frac{f_i}{f_i^*} \right) \quad (1.2)$$

where  $G_{fi}$  is Gibbs free energy of formation of  $i$ ,  $R$  is gas constant,  $f_i$  is the fugacity of  $i$ , and  $f_i^*$  is the fugacity of  $i$  in an ideal state.

Depending on the state of species, the chemical potential of species differs from the gas (g), liquid (l), and solid (s) states. This changes fugacity values and the following chemical potential to Equation 1.3:

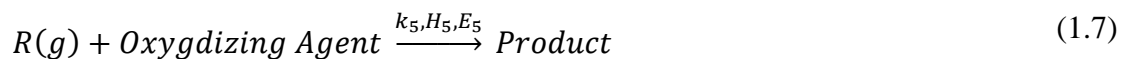
$$\mu_i^g = G_{fi}(T) + RT \ln \left( \frac{y_i P}{P^*} \right) \quad (1.3)$$

$$\mu_i^{s,l} = G_{fi}(T) + RT \ln \left( \frac{P^{sat}}{P^*} \right) + RT V_i^{s,l} (P - P^{sat}) \quad (1.4)$$

where  $y_i$  is the mole fraction of  $i$ ,  $P^*$  is the ideal gas pressure, and  $P^{sat}$  is the saturation pressure of  $i$ .

While the use of energetic species alone is a safety precaution, exhaust byproduct formation may lead to accumulation, which often makes matters worse due to the formation of

hotspots that restrict the cross-section of the exhaust line (Chang, 2019). During the deposition process, exhaust gases contain byproducts and unused precursors that are transported through an exhaust system, which is typically made of stainless steel or other materials that are resistant to corrosion and high temperatures. The exhaust system can experience hotspot formation because the conditions for chemical removal are different from those in the reactor or its downstream area. Then the deposit goes through oxidation to form an unintentional buildup in the downstream area. These phenomena can be generically shown in Equations 1.5 – 1.7:



where R is uncreated byproduct, k is rate of reaction, H is enthalpy of reaction, E is activation energy, Z is intermediate compound, and D is solid deposit formation after reaction.

Local hotspots can arise due to a variety of reasons, such as inadequate mixing of reactants, localized heating, hot spots generated from previous reaction steps, or the presence of impurities. This buildup can localize regional pressure and temperature buildups, exceeding the limitations of the proposed material stability. These hotspots can lead to a cascade of exothermic reactions that can result in thermal runaway and explosions, leading to significant safety and economic risks. Understanding the mechanisms and factors that contribute to the formation of hotspots is critical to designing safer and more efficient reaction processes in the chemical industry.

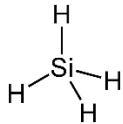
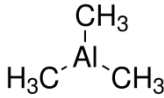
One approach to preventing the formation of hotspots is to initially ensure that the exhaust lines are designed with the appropriate cross-sectional area and materials, such as composites (Watson, 2020), that are resistant to high temperatures and corrosive environments. Another approach is to optimize the design of the exhaust system, such as by improving the

flow of exhaust gases by increasing the diameter of the downstream lines. Once the reaction that causes local hotspot formation is detected, these solutions can be implemented using monitoring and control systems. Overall, the formation of local hotspots by the restriction of cross-section in an exhaust line can have serious safety implications. It is important to design exhaust systems that minimize the risk of local hotspots and to implement monitoring systems to detect and prevent abnormalities in real-time.

### 1.3 Chemicals of Concern Related to Energetic Reactions

An energetic material is classified as a water-reactive and unstable material that is pyrophoric. Both silane and trimethyl-based precursors have characteristics of energetic materials that are prone to forming byproducts from deposition process reactions or excess from incomplete reactions. Since these precursors listed in Table 1.1 are noninterchangeable and are exemplary materials that are currently used in various semiconductor applications, the control and release of energetic materials or their byproducts are critical.

Table 1.1 Precursor properties and their safety information (based on reported material safety data sheets).

Category	Silane, SiH <sub>4</sub>	TMA, Al(CH <sub>3</sub> ) <sub>3</sub>
CAS Number	7803-62-5	92045-53-9
STP Phase	Gas	Liquid
Molar Mass (g/mol)	32.12	144.17
Melting Point (°C)	-185	15
Boiling Point (°C)	-112	125.5
Structure		
Hazard	Pyrophoric, compressed gas, flammable, acute toxicity, irritant	Pyrophoric, water reactive, corrosive

Silane serves as a silicon source for depositing silicon-based films, such as silicon oxide (SiO<sub>2</sub>) or silicon nitride (SiN<sub>x</sub>), which are essential for various electronic devices. Silane contains hydrogen atoms, which can contribute to hydrogen passivation and improve the electrical properties of the deposited films. Silane is also highly reactive and readily ignites given an energy source at temperatures below 54°C, making it suitable for chemical vapor deposition (CVD) processes. While its reactivity allows for controlled deposition and conformal coating of complex structures, the main concern comes from the highly unstable liquid or gaseous silanol SiH<sub>4-n</sub>(OH)<sub>n</sub> byproducts that are readily flammable (Category 2) and toxic (Category 4) (Choudhury, 2021). Figure 1.3 (a) shows the silane reaction pathway from pyrolysis, the H<sub>2</sub>O reaction, and the H<sub>3</sub>SiOH reaction. From the reaction pathways, Figure 1.3 (b) shows thermodynamically plausible deposit formation reactions, which have negative Gibbs free energies at 1 atm and 25 – 100°C conditions (HSC & Allendorf, 2002). With the exception of silicon dioxide formation, silanol production exhibited the most exothermic and therefore probable formation.

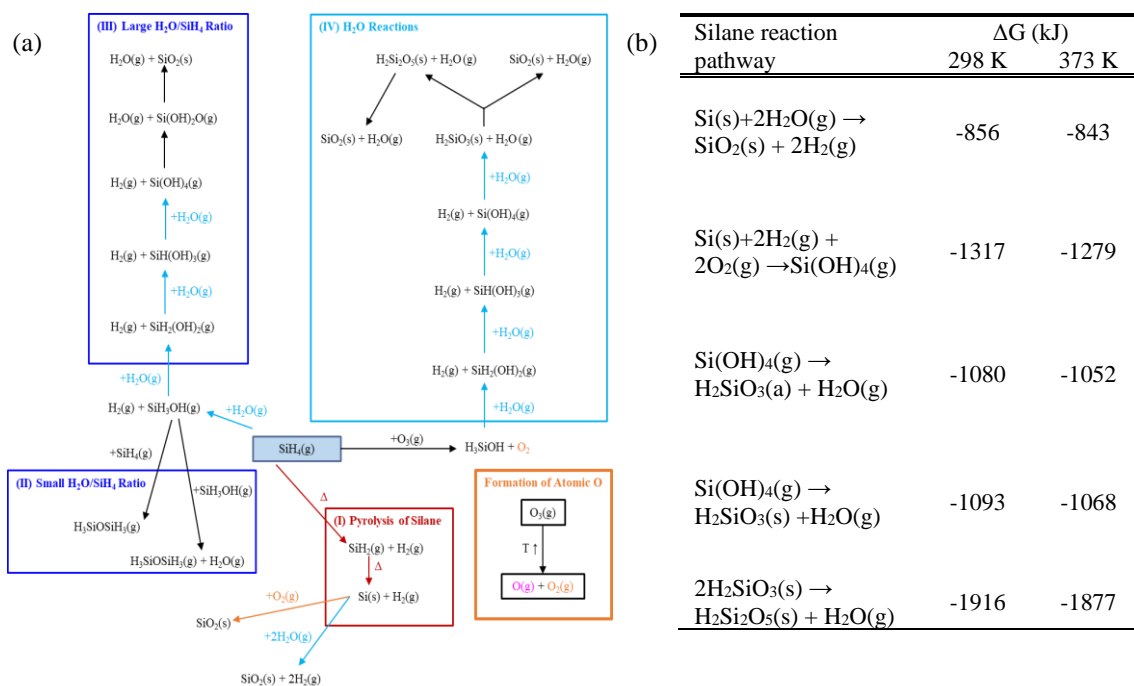


Figure 1.3 (a) Silane reaction pathway from pyrolysis, different ratio reaction with H<sub>2</sub>O, and reaction with H<sub>3</sub>SiOH (adapted Liu, 2022). (b) Calculated Gibb's free energy with silane that are exothermic reactions and potentially contribute to forming hazardous compounds (HSC and Liu, 2021)

TMA is an organometallic compound containing aluminum, a widely used material in semiconductor manufacturing. It serves as an aluminum source for depositing high-κ dielectric aluminum-containing films, such as Al<sub>2</sub>O<sub>3</sub>, at a value of ~9 (Sperling, 2020). TMA has a flash point of -7°C and an auto ignition point of 190°C, which is beneficial for low-temperature and deposition films on thermally sensitive substrates. TMA is particularly important in ALD processes, where its self-limiting reactions create precise, uniform, and conformal thin films. ALD allows for atomic-scale control of film growth and is essential for advanced semiconductor device fabrication. Figure 1.4 (a) shows the TMA reaction pathway from pyrolysis, reaction with O, and reaction with H<sub>2</sub>O. From the reaction pathways, Figure 1.4 (b) shows thermodynamically plausible deposit forming reactions, which have negative Gibbs free energies at 1 atm and 25 – 100°C conditions. These exothermic reactions produced aluminum carbide, carbonate, oxide, and hydroxide.



Table 1.2 Energetic species and their possible product between 25 – 100°C in exhaust lines (Liu, 2022). Compounds H<sub>2</sub> (g), H<sub>2</sub>O (l), H<sub>2</sub>O (g), O (g), O<sub>2</sub> (g), C (s), CO (g), and CO<sub>2</sub> (g) are found in all products of energetic species.

Energetic Species	Non-reactive solid	Possible contribution to fire hazard
SiH <sub>4</sub> (g)	Si SiO <sub>2</sub>	H <sub>2</sub> Si <sub>2</sub> O <sub>5</sub> (s) H <sub>2</sub> SiO <sub>3</sub> (s) H <sub>3</sub> SiOSiH <sub>3</sub> (g) Si(OH) <sub>4</sub> (l & g) SiH(OH) <sub>3</sub> (g) SiH <sub>2</sub> (OH) <sub>2</sub> (l & g) SiH <sub>3</sub> OH (l & g) SiH <sub>4</sub> (g)
TMA (l)	Al Al <sub>2</sub> O <sub>3</sub>	Al(CH <sub>3</sub> ) <sub>2</sub> (l) Al(CH <sub>3</sub> ) <sub>3</sub> (l) Al(OH) <sub>3</sub> (s) Al <sub>2</sub> (CH <sub>3</sub> ) <sub>6</sub> (l) Al <sub>2</sub> CO (s) Al <sub>4</sub> C <sub>3</sub> (s) AlCH <sub>3</sub> (l) AlO(OH) (s)

#### 1.4 Infrared Absorbance Studies of Thin Film Deposits

To monitor deposits forming with the precursor byproducts in the downstream area, an advanced analytical technique of Fourier transform infrared (FTIR) spectroscopy was employed. FTIR spectroscopy is an effective technique used to identify and quantify chemical species based on the absorption or transmission of infrared radiation by a sample. FTIR works by passing an infrared beam through a sample and measuring the amount of light absorbed by the sample (Ciurczak, 2021). Infrared radiation has a longer wavelength than visible light and is absorbed by molecules that undergo changes in their dipole moment when they vibrate. These vibrations are characteristic of the chemical bonds in a molecule and can be used to identify and quantify the types of bonds present in a sample. In a FTIR spectrometer, the infrared beam is first passed through an interferometer, which splits the beam into two separate beams. One of the beams is directed through the sample, and the other beam passes through a



reference material. The beams are then recombined and directed into a detector. The resulting interference pattern, known as an interferogram, contains information about the absorption spectrum of the sample. The interferogram is then transformed into a spectrum using the Fourier transform, which separates the complex interferogram into its individual frequencies.

When a molecule is exposed to IR radiation, it can absorb specific wavelengths that correspond to the thermal vibrational energy of its molecular bonds. The absorbed photon energy causes the bonds to vibrate, bend, and stretch in different ways, depending on the molecular structure and the types of bonds present. The resulting IR spectrum provides a unique absorption signal for the molecule, allowing for its identification and characterization. The interaction between light and molecular bonds is a resonance condition involving the transition between vibrational energy levels, and it can be understood with the harmonic oscillator equation of classical mechanics, known as Hooke's law (Larkin, 2011):

$$v = \frac{1}{2\pi} \sqrt{K \left( \frac{1}{m_1} + \frac{1}{m_2} \right)} \quad (1.8)$$

where  $v$  is vibrational frequency,  $K$  is force constant, and  $m_1$  and  $m_2$  are masses of each atom. The symmetry of the molecule is another factor to consider when it comes to observing absorption spectra because it limits the detection of only stretching and bending modes of dipole interaction between molecules.

To analyze a solid sample, two distinct types of IR spectroscopies are often used. The attenuated total reflectance (ATR) FTIR incorporates an internal reflective element crystal that comes into direct contact with the material. In this process, infrared light is directed and internally reflected within the crystal, causing an orthogonal evanescent wave to penetrate the sample surface. ATR FTIR is useful because it requires minimal sample preparation, making it suited for the investigation of liquids, solids, and uneven surfaces. However, its drawback is the short penetration depth, which normally ranges between 1 and 2 micrometers. Absorbance

FTIR, on the other hand, requires subjecting the sample to an infrared beam, which is typically in the form of a solution, dispersion in a solvent, or fine powder combination. The transmitted light is then measured, and the resulting spectrum shows how the sample absorbs specific wavelengths. While absorbance FTIR allows for a wider variety of sample types, it frequently necessitates more sample preparation than ATR FTIR. The choice between both methods is influenced by factors such as the nature of the sample, the desired depth of analysis, and the level of sample preparation convenience required for a certain application. Because the study requires finding byproduct thin films with a high refractive index and nonuniform thickness, absorbance FTIR was chosen.

In the literature, extensive analyses of inorganic absorbance spectra have been carried out, with a special emphasis on thin film depositions such as  $\text{SiO}_2$  (Han, 1996) and  $\text{Al}_2\text{O}_3$ . (Goldstein, 2008) The purpose of these investigations is to pinpoint the unique vibrational functional peaks connected to these thin films. Through the analysis of absorbance spectra, a thorough grasp of the molecular makeup and structural properties of these inorganic films can be determined, which aids their applications in a variety of domains, including materials science and semiconductor production.

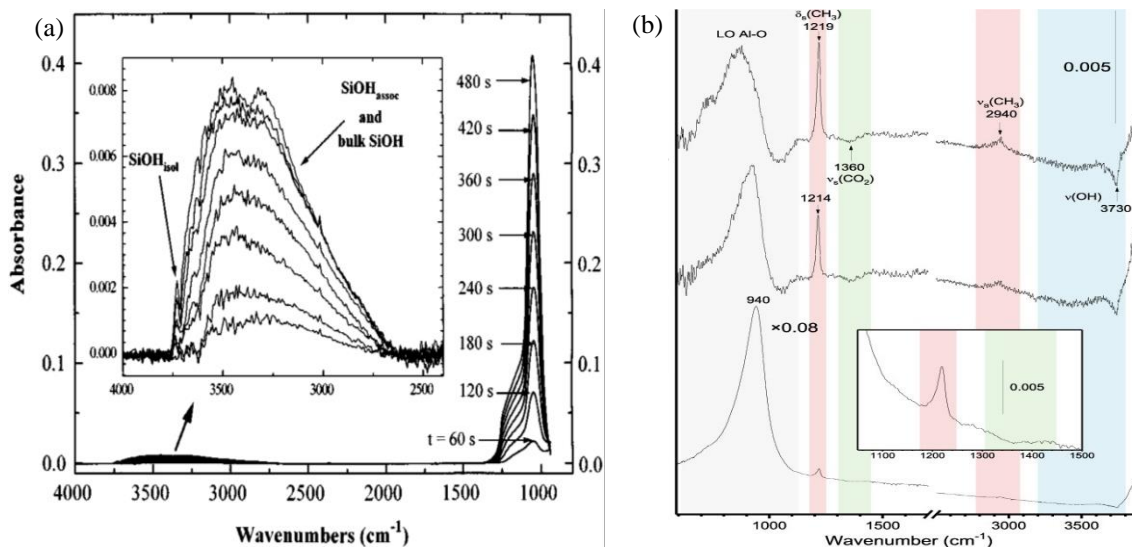
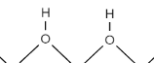
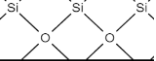
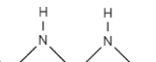
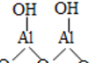
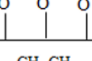
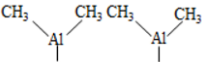

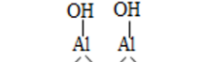
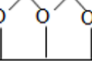


Figure 1.5 (a) Absorption spectra of SiO<sub>2</sub> with varying time using Fourier transform infrared (FTIR) spectroscopy. The plasma-enhanced chemical vapor deposition was kept at RF power of 100 W, substrate temperature of 250 °C, 25 mTorr, and gas flowrate of 50 sccm (adapted from Han, 1996). (b) Absorption spectra of Al<sub>2</sub>O<sub>3</sub> FTIR absorbance scans with different cycles of 0.5 s trimethyl aluminum (TMA)/H<sub>2</sub>O atomic layer deposition at 103°C (adapted from Sperling, 2020).

The degree of freedom (DOF) is an important concept that refers to the number of ways in which a molecule can vibrate. The DOF determines the number and frequency of the molecular vibrations that can be detected in the sample (Ciurczak, 2021). This phenomenon is closely related to the number of atoms in the molecule and the ways in which they are connected. For example, a diatomic molecule of CO has only one DOF because it can only vibrate along the bond axis. It is important to address this matter, as the DOF in FTIR spectroscopy determines its ability to provide information about the functional groups present in the samples. Each functional group has a characteristic set of molecular vibrations that can be detected by FTIR spectroscopy, and the number and frequency of these vibrations are related to the degree of freedom of the molecule. By analyzing the FTIR spectra of a sample, it is possible to identify the functional groups present and gain insights into the chemical structure and composition of the sample. Table 1.3 contains a list of literature vibrational wavenumbers from silicon, aluminum, and hafnium compounds that were identified in the FTIR analysis to

detect the unknown byproducts from plasma-enhanced chemical vapor deposition (PECVD) and atomic layer deposition (ALD) tools.

Table 1.3 Literature reported vibrational wavenumbers of surface species involving Si, Al, Hf, O, N, C, and H.

Regions	Bond surface	Wavenumber (cm <sup>-1</sup> )	Reference
Si-OH stretch		3800-3600	(1)
O-H stretch		3700-3250	(1)
N-H stretch	SiN <sub>x</sub> surface	~3350	(2)
Si-H stretch	Si surface	~2150	(2)
N-H bend		1200-1150	(2)
Si-O stretch	Si surface	1110-1050	(1)
Si-N stretch	Si surface	960-830	(1)
Si-O bend	Si surface	820-790	(1)
Si-O rock	O-Si-O surface	~450	(1)
Al-OH stretch		3800-3650	(3)
O-H stretch		3750-3600	(3)
C-H stretch		2980-2800	(4)
C-H bend		2900-2800	(4)
CH <sub>3</sub> deformation		~1400	(4)
Al-O bend		800-710	(5)
Hf-OH stretch	O surface	3800-3650	(6)
Hf-O bend	O surface	800-710	(6)

- (Han and Adyil, 1996)
- (Nakamoto, 2009)
- (Ludwig and Burke, 2022)
- (Nyquist and Kagel, 1971)
- (Ludwig and Burke, 2022)
- (Ho, Wang, Brewer, Wielunski, Chabal, Moumen, and Boleslawski, 2005)

## 1.5 Scope and Organization

The scope of this study is to investigate and monitor byproduct formation in the downstream area of deposition tools. Specifically, the examination of byproducts associated with the employment of silane, trimethyl aluminum, and tetrakis (dimethyl amido) hafnium chemistries is explored using PECVD and ALD tools. Integrated with *in-situ* and *ex-situ* FTIR

spectroscopies as well as XPS, the material characterization of byproduct constituents is highlighted. Identification of byproducts in the exhaust lines can be applied to the best-known methods and standard operating procedures to reduce the risk of safety.

## CHAPTER 2: EXPERIMENTAL SETUP

This chapter discusses the experimental approach to monitor the chemical reactions taking place in the downstream areas of two deposition systems: a plasma-enhanced chemical vapor deposition reactor and an atomic layer deposition, using silane, trimethyl aluminum, and  $\text{Hf}(\text{NMe}_2)_4$ , for the deposition of oxide and nitrides. Both *in-situ* and *ex-situ* analyses by Fourier transform infrared spectrometry and *ex-situ* X-ray photoelectron spectroscopy offer complementary chemical information about the thin film information in the exhaust lines of these tools. Experimental results from combining monitoring deposition tools and analyzing spectroscopies can help mitigate the environment impact and supply a safer workplace for employees.

### 2.1 Exhaust Monitoring of Deposition Chambers

#### 2.1.1 Plasma-Enhanced Chemical Vapor Deposition Chamber

PECVD involves the use of plasma, which is a state of matter similar to a gas but with some ions and electrons present. Plasma can be generated by applying a high voltage to a gas, which ionizes the gas and creates plasma. During PECVD, the substrate is placed in a vacuum chamber, and a gas mixture is introduced. The gas mixture typically contains a precursor gas and a carrier gas, which helps transport the precursor to the substrate. The plasma helps break down the precursor gas and deposit it onto the substrate in a controlled manner. The parameters of the PECVD process, such as the gas flow rate, pressure, and power of the plasma, can be adjusted to control the properties of the deposited film, such as its thickness, composition, and structure.

As shown in Figure 2.1 (a), the PECVD reactor (maker, model) typically operates at 500 mTorr, 300°C, 30 – 50 W, 30 sccm of  $\text{SiH}_4$ , and 4.0 DC bias. As shown in Table 2.1, it uses silane, nitrous oxide and ammonia precursors to deposit  $\text{SiO}_2$  and  $\text{SiN}_x$ , while  $\text{SF}_6$  is used for

chemical cleaning of the reactor surfaces. In the PECVD exhaust line, a FTIR spectrometer (Figure 2.1 (b)) is connected via ISO-63 K adaptor tee (Appendix 1.3) to allow for *in-situ* analysis of the deposition formation in the exhaust line.

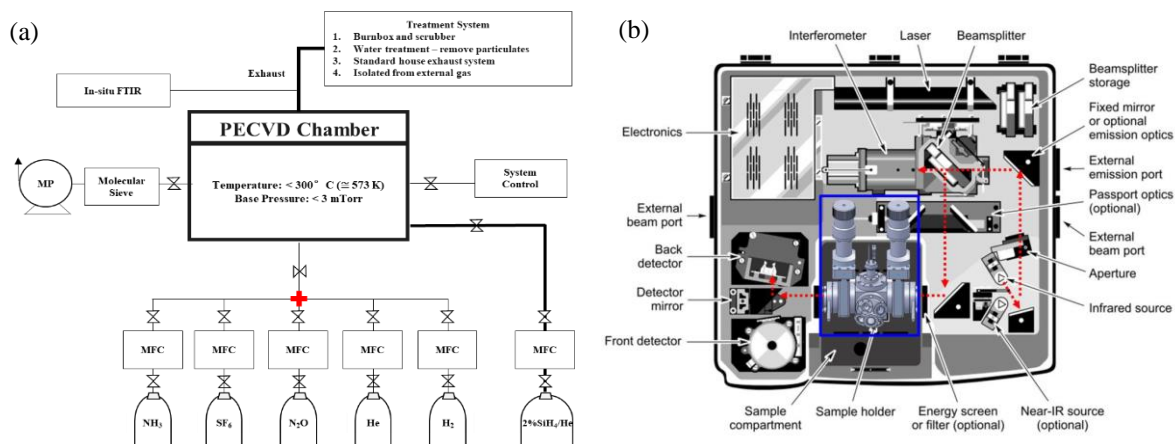


Figure 2.1 (a) A schematic diagram of a plasma-enhanced chemical vapor deposition (PECVD) tool used in this work, with *in-situ* Fourier transform infrared (FTIR) spectroscopy implemented in the exhaust for monitoring. (b) A top view illustration of the *in-situ* FTIR chamber for in-line monitoring of the PECVD thin film deposition process in the exhaust line (adapted from Cho, 2015).

Table 2.1 Precursors used in the plasma-enhanced chemical vapor deposition system and their properties as listed in the material safety data sheet (MSDS).

Category	$\text{SiH}_4$	$\text{N}_2\text{O}$	$\text{NH}_3$	$\text{SF}_6$
CAS Number	7803-62-5	10024-97-2	92045-53-9	2551-62-4
STP Phase	Gas	Gas	Gas	Gas
Melting Point ( $^{\circ}\text{C}$ )	-185	-90.9	-77.7	-64.0
Boiling Point ( $^{\circ}\text{C}$ )	-112	-88.5	-33.3	-50.8
Structure				

### 2.1.2 Atomic Layer Deposition Chamber

The ALD is a cyclic process that uses sequential alternating exposure of self-limiting precursor reactions to the substrate surface. The precursor adsorbs onto the surface in a self-limiting monolayer where excess is removed. Subsequently, the substrate is exposed to a

second precursor, which reacts with the first deposited monolayer thin film and terminates when the substrate surface is saturated. This self-limiting nature enables precise control of film thickness and composition on a nanoscale. The process is repeated for a desired number of cycles to build up a thin film of the desired thickness.

As shown in Figure 2.2, a Ultratech Fiji ALD is used in this work and the typical operating conditions are 0.02 mTorr, 300 – 400°C, 300 W, and 20 sccm flow rate for both  $\text{Al}(\text{CH}_3)_3$  and  $\text{Hf}(\text{NMe}_2)_4$ . As shown in Table 2.2, it mainly uses cycles of  $\text{Al}(\text{CH}_3)_3/\text{H}_2\text{O}$  and  $\text{Hf}(\text{NMe}_2)_4/\text{H}_2\text{O}$  to respectively deposit  $\text{Al}_2\text{O}_3$  and  $\text{HfO}_2$ , while no cleaning gas is used. All organometallic precursors used in the ALD system is tabulated in Table 2.2, and water vapor that is used in thermal cyclic pulse is not shown.

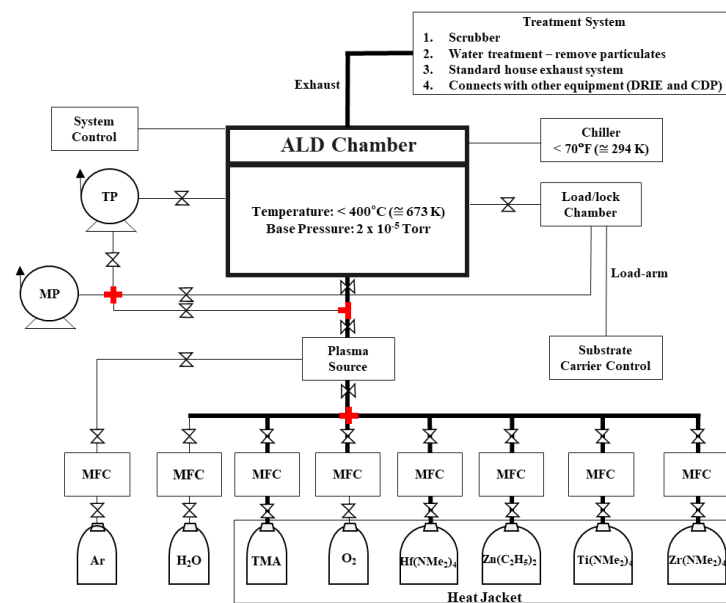
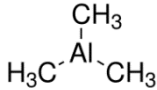
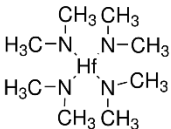
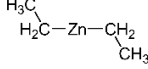
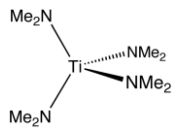
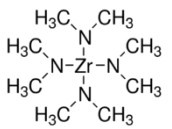


Figure 2.2 A schematic diagram of an atomic layer deposition (ALD) tool used in this work.



Table 2.2 Precursors used in the atomic layer deposition (ALD) system and their properties as listed in the material safety data sheet (MSDS).

Category	Al(CH <sub>3</sub> ) <sub>3</sub>	Hf(NMe <sub>2</sub> ) <sub>4</sub>	Zn(C <sub>2</sub> H <sub>5</sub> ) <sub>2</sub>	Ti(NMe <sub>2</sub> ) <sub>4</sub>	Zr(NMe <sub>2</sub> ) <sub>4</sub>
CAS Number	92045-53-9	19782-68-4	557-20-0	3275-24-9	19756-04-8
STP Phase	Liquid	Solid	Liquid	Liquid	Solid
Melting Point (°C)	15	26 – 29	-28	NA	57-60
Boiling Point (°C)	125.5	NA	117	50	NA
Structure					

### 2.1.3 Monitoring System

The schematic of the experimental monitoring system is shown in Figure 2.3. Each deposition tool has a reactor or deposition chamber that can directly grow thin films with the provision of the necessary precursors. In this chamber, a growth experiment is held to directly deposit thin film on a KBr pellet to acquire upstream products. The *in-situ* FTIR or FTIR experiment is only available at the PECVD due to the physical space limitation in ALD cleanroom site. The *in-situ* FTIR is attached at the downstream and bypasses exhaust via an ISO-63 K adaptor tee (Figure 2.3 (b)). The attached analysis tool is a modified version of *in-situ* 670 FTIR, which has a sample holder to place the KBr pellet inside. This setup enables real time IR analysis of downstream byproduct buildup on the pellet. The exhaust monitoring experiment is available for both tools, where KBr pellets are placed inside the exhaust lines and extracted with a schedule for long term accumulation observation.

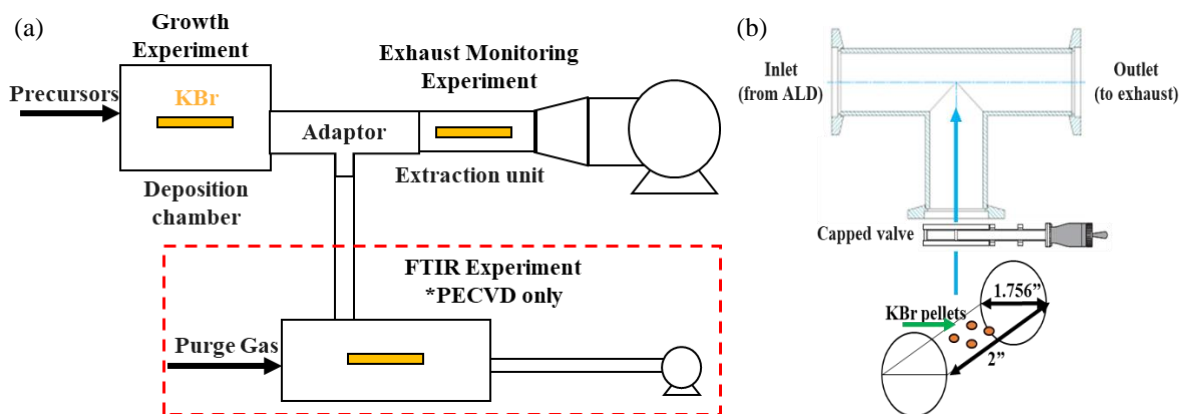


Figure 2.3 (a) A schematic diagram of experimental setup with the KBr locations indicated. Currently, only plasma-enhanced chemical vapor deposition has implemented an *in-situ* Fourier transform infrared setup, while the atomic layer deposition exhaust line is interconnected with three other tools. (b) The adaptor tee schematic attached exhaust lines to with stainless steel mesh pellets to place KBr pellets in the downstream lines.

#### 2.1.4 Potassium Bromide Pellet

In order to monitor the thin film deposition by *in-situ* and *ex-situ* FTIR, potassium bromide (KBr) pellets were made to measure the absorbance spectrum and identify the composition of accumulating substances in the deposition tool exhaust. The KBr pellet is an ideal substrate because it is transparent in IR wavenumber region ( $4000 - 400 \text{ cm}^{-1}$ ). Besides the nature of KBr being hygroscopic, measuring FTIR scans with KBr pellets can identify products that adhere to the pellet. Another application of KBr pellets used in FTIR spectroscopy can be easily seen by mixing and grinding the sample with KBr powder during the creation of the pellet. This results in a thin, uniform sample that is easy to handle and insert into the FTIR instrument. Additionally, the KBr does not absorb infrared radiation at frequencies of interest, so it does not interfere with the sample's spectrum. Overall, KBr pellets offer a simple, low-cost, and reliable method for preparing samples for FTIR analysis.

For the creation of the pellet, the KBr powder was purchased from International Crystal Laboratories with a CAS number of 7758-02-03. Initially, using a mortar and pestle, 140 mg of KBr powder is ground finely to create a uniform pellet surface. Then a 13 mm pellet die set

was configured to receive the KBr powder in Figure 2.4 (a). The die set configuration was pressed with a hydraulic press with 10,000 lb force for 3 minutes. After gently removing the pellet, the front side is engraved with a blade to indicate the side of the pellet that faces the center of the exhaust of a deposition tool. Finally, the KBr pellet was weighed with a mass balance, and the individual pellet weight was monitored through the monitoring and deposition process. As shown in Figure 2.4 (b), the initial weights of the KBr pellets were ~8 mg less than those of the powder used, but they were comparable to each other before inserting them in locations of interest.

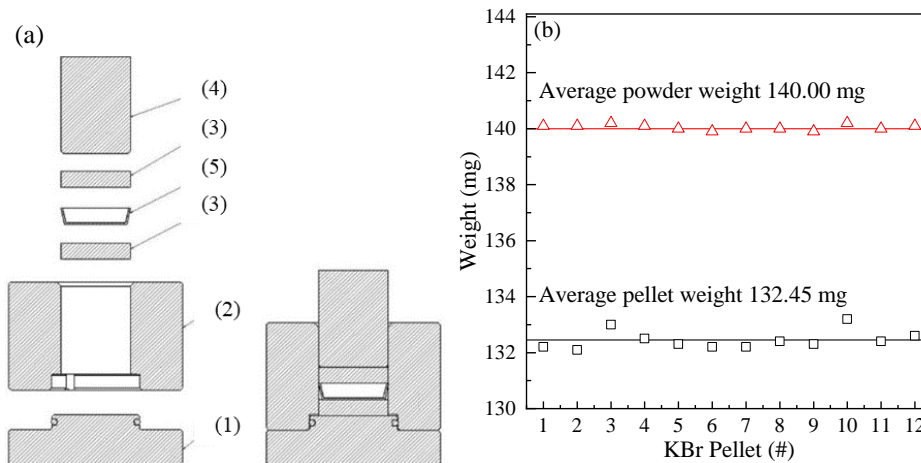


Figure 2.4 (a) 13mm pellet die set schematic with (1) die base, (2) die body, (3) die pellets, (4) plunger, and (5) sample holder (adapted from Chemplex®, 2019). To create an infrared transparent pellet, place 140 mg KBr powder (5) and assemble the die set before applying 10,000 lb with hydraulic press (Appendix 3). (b) Variation of twelve as-made KBr pellet masses and their corresponding initial KBr powder masses.

Since the amount of deposits results in small mass increase, a precise initial mass measurement for each pellet is required for proper referencing. Depending on the location, the pellet was exposed to the gas flow of precursor in the deposition chamber or in the exhaust, resulting in mass accumulation on the pellets. After the process, the KBr pellet was removed from the monitoring environment, and a precise mass balance was performed to calculate the weight gain due to the deposits. A positive change in weight indicates deposition occurred. A

negative change in weight could suggest loss of material, either from the sample itself or from the KBr pellet, which can happen due to factors like mechanical stress or evaporation during handling. As handling and contamination are major factors in weight deviation, the utmost care was required to accommodate for thin deposition.

For the context of the following experiments, the entire KBr pellets that were placed deposition chamber, *in-situ* FTIR, and exhaust of a deposition tools employed a naming convention that are shown in Table 2.3. The different pellet IDs for both tools encompass details like exposure duration and the particular deposition processes that precede extraction. The total exposure time serves as an indicator for FTIR analysis, and the last process before extraction has the most influence on the surface sensitive analysis by XPS.

Table 2.3 The pellet ID naming scheme used in this work, where (i), (ii), (iii), (iv) stands for pellets extracted from the exhaust lines in a sequential order, typically one month apart, and (Ref) is each corresponding as-prepared KBr pellet. For each sample, the exposure time to the precursors and the last process before extraction are also listed.

Pellet ID	PECVD		ALD	
	Exposure time of SiH <sub>4</sub> , N <sub>2</sub> O, NH <sub>3</sub> , SF <sub>6</sub> (hr)	Last process before extraction	Exposure time of Al(CH <sub>3</sub> ) <sub>3</sub> , Hf(NMe <sub>2</sub> ) <sub>4</sub> , H <sub>2</sub> O (hr)	Last process before extraction
(Ref)	As prepared KBr reference			
(i)	17, 7, 10, 11	1.5 hours of SiH <sub>4</sub> /N <sub>2</sub> O	127, 8, 135	0.5 hours of Al(CH <sub>3</sub> ) <sub>3</sub> /H <sub>2</sub> O
(ii)	13, 6, 7, 9	3 hours of SF <sub>6</sub>	118, 6, 124	3 hours of Al(CH <sub>3</sub> ) <sub>3</sub> /H <sub>2</sub> O
(iii)	7, 5, 2, 0	0.5 hour of SiH <sub>4</sub> /NH <sub>3</sub>	12, 2, 14	3 hours of Hf(NMe <sub>2</sub> ) <sub>4</sub> /H <sub>2</sub> O
(iv)	3, 2, 1, 4	2 hours of SF <sub>6</sub>	4, 2, 6	2 hours of Hf(NMe <sub>2</sub> ) <sub>4</sub> /H <sub>2</sub> O

## 2.2 Material Characterization Techniques

### 2.2.1 Fourier Transform Infrared Spectroscopy

The FTIR technique is an effective technique that can identify vibrational nodes in samples when an infrared source ( $\lambda$ : 25 - 2.5  $\mu\text{m}$ ) is radiated. The vibrational nodes resonate with the IR wavelength, where samples absorb photon energy to provide characteristic transmission or absorption peaks (B. H. Stuart, 2005). Table 2.4 summarizes the different specifications between two FTIR spectrometers that were utilized for *in-situ* and *ex-situ* analysis.

For *in-situ* measurements, a Nexus 670 FTIR spectrometer from Thermo Nicolet with germanium (Ge) on a cesium iodide (CsI) beam splitter and a deuterated triglycine sulfate (DTGS) pyroelectric IR detector were used to collect FTIR spectra. This FTIR has a customized chamber with a 2.75'' OD six-way cube attached to two 2.75'' OD gate valves (Cho, 2015) where substrates can be located between the windows of the beam source and detector. The chamber and exhaust of the PECVD were also modified for connection. The use of a CsI beam splitter and DTGS detector allows the detection of IR wavenumbers from 4000  $\text{cm}^{-1}$  to 400  $\text{cm}^{-1}$ . In this region, detailed surface mechanisms and processes can be studied by analyzing the IR responses of the surface hydroxyl (4000 – 3800  $\text{cm}^{-1}$ ) and C-H stretching (3000 – 2800  $\text{cm}^{-1}$ ) regions. The spectrometer setup was purged with dry  $\text{N}_2$  and  $\text{CO}_2$  from a purge gas generator.

The *ex-situ* measurements utilized a Thermo Nicolet Nexus 8700 FTIR spectrometer. Combination of potassium bromide (KBr) window and mercury cadmium telluride (MCT) can detect IR wavenumbers from 5000  $\text{cm}^{-1}$  to 400  $\text{cm}^{-1}$ . For both measurements spectra were collected with a mirror speed of 3.6  $\text{cm/s}$  and averaged over at least 128 scans using 4  $\text{cm}^{-1}$  resolution. All spectra were normalized using the background scan on the initial starting substrate.

Table 2.4 Different specification of Nexus Thermo Nicolet Fourier transform infrared (FTIR) spectroscopies that were used. *In-situ* 670 FTIR has custom built chamber and is attached to the exhaust of plasma-enhanced chemical vapor deposition reactor. *Ex-situ* 8700 FTIR uses KBr beams splitter, MCT detector, and IR source to simulate conditions of *in-situ* FTIR.

Category	<i>In-situ</i> 670 FTIR	<i>Ex-situ</i> 8700 FTIR
Beam splitter	CsI (400 – 4000 cm <sup>-1</sup> )	Quartz (3,300 – 25,000 cm <sup>-1</sup> ) KBr (400 – 5000 cm <sup>-1</sup> ) CaF <sub>2</sub> (1,200 – 15,000 cm <sup>-1</sup> )
Detector	DTGS (400 – 10,000 cm <sup>-1</sup> )	InSb (1,850 – 10,000 cm <sup>-1</sup> ) MCT (450 – 11,700 cm <sup>-1</sup> )
Source	IR (600 – 4000 cm <sup>-1</sup> )	IR (600 – 4000 cm <sup>-1</sup> ) White light (12,500 – 25,000 cm <sup>-1</sup> )
Software	OMNIC	OMNIC

With the goal of accurately interpreting the absorbance scans of KBr pellets after deposition, a solid reference baseline must be established. To demonstrate the reproducibility and establish the baseline for each KBr pellet, Figure 2.5 (a) shows twelve KBr pellets and their respective absorbance scans. The scans were carried out to capture the inherent properties of the KBr material without interference from other sources. The spectrum of KBr's intrinsic absorbance properties and the background condition with nitrogen purging are clearly shown in the reference scan, making it possible to identify and analyze subsequent scans with accuracy. The KBr pellets have consistent CO<sub>2</sub>, H<sub>2</sub>O, and organic features that are present in the environment. These initial reference scans guarantee that any differences seen in the next scans are ascribed to the particular properties of the deposited films, enabling a thorough comprehension of the interaction between the films and the KBr substrate. To identify the differences, subtraction of background can be done as shown in Figure 2.5 (b). The KBr reference spectrum subtracted by the as-taken data, demonstrates signal intensities that comes from byproducts of SiO<sub>2</sub> and SiN<sub>x</sub> deposition process from 7 hours of SiH<sub>4</sub>, 5 hours of N<sub>2</sub>O, and 2 hours of NH<sub>3</sub>.

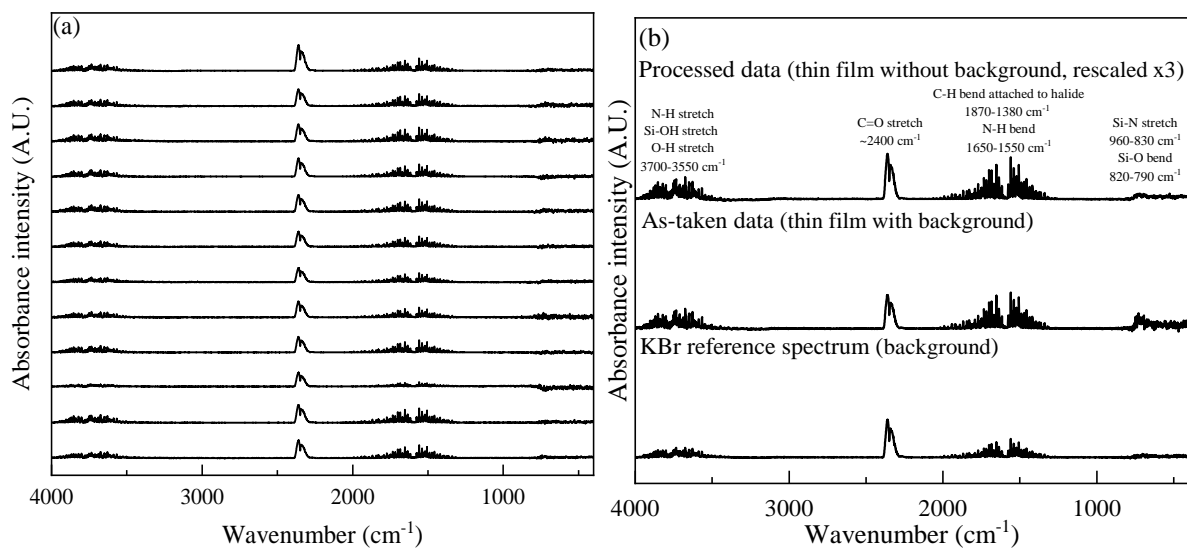


Figure 2.5 (a) Absorbance infrared spectra of twelve KBr pellets as references for post-deposition analysis. (b) The thin film deposition features from as-taken data of 7 hours of SiH<sub>4</sub>, 5 hours of N<sub>2</sub>O, and 2 hours of NH<sub>3</sub> in plasma-enhanced chemical vapor deposition exhaust was subtracted with reference KBr spectrum presented in the bottom spectrum of (a). This processed data was rescaled by 3 times and signals attribute to just IR traces of thin film deposits.

To integrate the intensity of specific absorption peaks in FTIR, absorption spectra require several prerequisite steps. The initial step is to correct the background baseline by removing shift and noise, resulting in more accurate background data. Once the background is adjusted, two different spectra are subtracted from one another to only show peaks of interest. Following subtraction, peak area integration is performed using OMNIC software's built-in mathematical approaches such as the trapezoidal rule. It is crucial to note that the ranges supplied for O-H, Si-OH, and M-OH stretching modes are only approximations of where these functional groups may show absorption peaks in the spectra. Given the difficulty of distinguishing O-H, Si-OH, and M-OH peaks solely from their absorption peaks in the FTIR spectrum, all intensities within the specified range are integrated after spectra subtraction. This inclusive approach ensures that all relevant absorption contributions are accounted for, even if they cannot be clearly assigned to a specific functional group. Similarly, for other functional groups such as Si-N, Si-O, and

M-O, the integration process entails adding the intensities within their respective characteristic ranges. This recognizes the difficulty of distinguishing between these groups in complex spectra and ensures a thorough evaluation of functional group contributions. Overall, the integration process includes background correction and the summation of intensities within specified ranges to capture the contributions of various functional groups.

## 2.2.2 X-ray Photoelectron Spectroscopy

X-ray photoelectron spectroscopy (XPS) is an analytical technique used to determine the chemical composition and oxidation state of a material's surface. XPS involves the photoelectric effect of irradiating the surface of a material with X-rays, which causes the ejection of photoelectrons. By measuring the kinetic energy (KE) and number of ejected electrons, XPS can identify the elemental composition and chemical state of the surface. Due to the limited mean free path of the photoelectrons, XPS can be used to analyze ~ 10 nm of surface materials, including metals, semiconductors, polymers, and biological samples. The binding energy measured provides information on the element, oxidation state, chemical bonding, as they all depend on its molecular environment using Equation 2.1:

$$KE = h\nu - BE - \Phi \quad (2.1)$$

where  $h\nu$  is incident photon energy,  $BE$  is binding energy, and  $\Phi$  is the spectrometer work function. Utilizing the technique is beneficial to quantify concentrations on the surface and deduce possible components that build up in the downstream area.

In this work, an XPS system (Kratos, DLD Axis Ultra) was used with an Al anode source (1486.6 eV) and a 90° or perpendicular takeoff from the sample surface. While the survey spectra were observed with 160 eV pass energy and 1 eV step size, the detailed high-resolution scans were obtained with 20 eV pass energy and 0.1 eV step size. All spectra were referenced to the advantageous carbon peak of C-C bonding in the C1s spectra at 284.8 eV binding energy.



As an example, Figures 2.6 (a) and (b) are XPS survey scans from respective chamber deposited with SiO<sub>2</sub> and Al<sub>2</sub>O<sub>3</sub>. The SiO<sub>2</sub> scan has elements of O, K, C, Br, and Si, while the Al<sub>2</sub>O<sub>3</sub> scan has elements of O, F, K, C, Al, and Br.

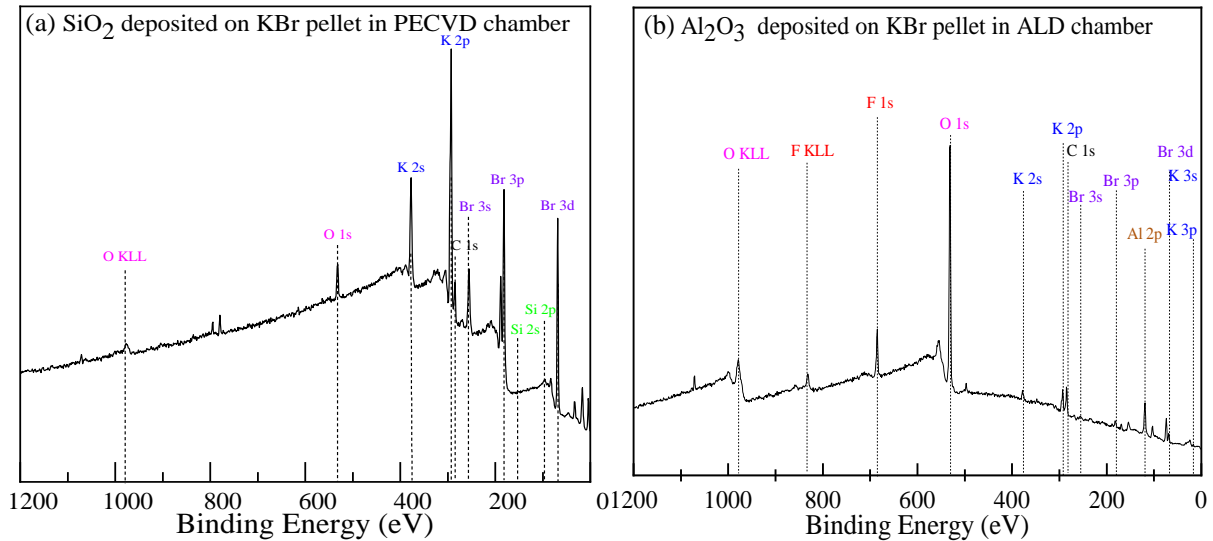


Figure 2.6 (a) A XPS survey spectrum obtained from SiO<sub>2</sub> deposition on a KBr pellet inside the plasma-enhanced chemical vapor deposition reactor. (b) A survey XPS spectrum obtained from Al<sub>2</sub>O<sub>3</sub> on a KBr pellet inside the atomic layer deposition reactor.

Subsequently, XPS can also be used to study changes in the surface composition and chemistry. The atomic composition analysis of the surface material was calculated using the integrated intensities of an element and the relative sensitivity factor or normalization of the photoemission peaks using the Kratos XPS library.

$$\alpha_i = \frac{A_i / RSF_i}{\sum_{i=1}^n A_i / RSF_i} \quad (2.2)$$

where A is the peak area of integrated intensity and RSF is the relative sensitivity factor for the element i. The entire set of elements that were identified in this study are tabulated in Table 2.5 with corresponding species, binding energy, spin orbital splitting, and RSF. Also, by analyzing the integrated peak area ratios, the identified elements can be recognized into species and compositions for consideration.

Table 2.5 Relative sensitivity factor (RSF) values of elements used in X-ray photoelectron spectroscopy (XPS) measurement. (Biesinger, 2021).

Element	Species	Binding Energy (eV)	Spin Orbital Splitting(eV)	RSF
F	Metal fluoride	685.0 ( $\pm$ 0.9)	-	1.000
	SF <sub>6</sub>	690.3 ( $\pm$ 1.7)		
O	SiO <sub>2</sub>	532.9 ( $\pm$ 0.4)	-	0.780
	Al <sub>2</sub> O <sub>3</sub>	531.0 ( $\pm$ 1.0)		
	HfO <sub>2</sub>	531.0 ( $\pm$ 1.0)		
	Hydroxides	531.3 ( $\pm$ 0.3)		
	Organic	531.3 ( $\pm$ 0.3)		
	SiH <sub>4-x</sub> (OH) <sub>x</sub>	534.1 ( $\pm$ 0.8)		
N	Si <sub>3</sub> N <sub>4</sub>	397.8 ( $\pm$ 0.5)	-	0.477
K	KF	282.8 ( $\pm$ 0.3)	2p 3/2 – 1/2 (2.77 – 2.8)	1.466
	K <sub>2</sub> SO <sub>4</sub>	292.9 ( $\pm$ 0.6)		
	KBr	293.0 ( $\pm$ 0.1)		
C	C-C, C-H	284.8	-	0.278
	C <sub>x</sub> -F <sub>y</sub>	285.3 ( $\pm$ 1.0)		
	C-O-C	286.3 ( $\pm$ 1.7)		
	C=O	287.8 ( $\pm$ 3.0)		
	O-C=O	288.8 ( $\pm$ 4.3)		
S	SO <sub>4</sub> <sup>2-</sup>	168.9 ( $\pm$ 0.6)	2p 3/2 – 1/2 (1.18)	0.668
Si	SiH <sub>4-x</sub> (OH) <sub>x</sub>	101.1 ( $\pm$ 0.9)	2p 3/2 – 1/2 (0.6)	0.328
	SiN <sub>x</sub>	101.7 ( $\pm$ 0.5)		
	SiO <sub>2</sub>	103.5 ( $\pm$ 0.3)		
Al	Al	72.7 ( $\pm$ 0.3)	2p 3/2 – 1/2 (0.44)	0.193
	Al <sub>2</sub> O <sub>3</sub>	74.1 ( $\pm$ 1.0)		
Br	KBr	68.7 ( $\pm$ 0.2)	3d 5/2 – 3/2 (1.05)	1.055
Hf	HfO <sub>2</sub>	17.5 ( $\pm$ 0.7)	4f 7/2 – 5/2 (1.71)	2.639
	Hf	14.3 ( $\pm$ 0.1)		

### 2.3 Summary

The experimental setup included ex-situ FTIR analysis of thin film growth inside PECVD and ALD tools as well as the thin film accumulation in both exhaust lines, using a designed sample extraction system. The in-situ FTIR analysis was only available in the PECVD system, serving to bridge the ex-situ measurements made the in reaction and that in the exhaust line. Complementary results from XPS help provide extensive information on the elemental composition and chemical states. When combined, these methods aid in the understanding of

the characteristics of the formation of reaction byproducts in the exhaust line of deposition tools.

### CHAPTER 3: MONITORING AND ANALYSIS OF PECVD SYSTEM

This chapter summarizes three different experiments conducted in a plasma-enhanced chemical vapor deposition tool, utilizing different ratios of silane, nitrous oxide, and ammonia for silicon dioxide and nitride depositions. This deposition tool has a chemical cleaning procedure with sulfur hexafluoride to remove extraneous deposition and byproduct residue in the chamber. The typical thin films deposited in the reactor had distinct features such as Si-O stretching, and Si-N bending found in silicon dioxide and nitride. The *in-situ* Fourier transformation infrared spectroscopy analyses organized simultaneously with the chamber growth experiment showed similar features but reduced signal intensity, with fewer organic substances, due to the reduced temperature in the downstream area. By monitoring the cumulative chemical effect in the exhaust line on a monthly basis, the chemical composition of the deposits in the downstream area was uncovered. The absolute mass of deposits on each extracted pellet increased over time as more precursors and reaction byproducts deposited on the pellets. As the processing time involving SiH<sub>4</sub>, N<sub>2</sub>O, and NH<sub>3</sub> increased, amplified vibrational peaks were easily distinguished: silicon dioxide and nitride composition were found in addition to both stretching nodes of O-H at ~3700 cm<sup>-1</sup> and Si-OH at 3652 cm<sup>-1</sup> from silanol. Also, the X-ray photoelectron spectroscopy analyses showed an increase in relative atomic concentrations of oxygen 1s and silicon 2p binding energy peaks with additional exposure to precursors, consistent with the formation of silanol. The byproduct composition on the surface had its silicon composition reduced with chemical cleaning, such that timely cleaning must be administered to avoid deposition buildup on the exhaust surface.

### 3.1 Growth Experiment in PECVD Chamber

In this study, direct chamber thin film growth was done by depositing silicon dioxide ( $\text{SiO}_2$ ) and silicon nitride ( $\text{SiN}_x$ ) directly onto KBr pellets. The aim was to lay the groundwork for identifying distinctive peaks of  $\text{SiO}_2$  and  $\text{SiN}_x$  films and assigning the observed peak features for the following experiments. Direct deposition of  $\text{SiO}_2$  and  $\text{SiN}_x$  onto KBr pellets served as an effective means of providing valuable insights for further characterization and analysis. Thin film deposits have their own signature features that can be identified with both IR responses and XPS scans.

On a KBr pellet, a 1  $\mu\text{m}$  thin film of  $\text{SiO}_2$  or  $\text{SiN}_x$  was grown and went through FTIR absorbance spectra scans. Each absorbance scan was averaged after taking five scans and subtracted from its corresponding KBr background spectra. The  $\text{SiO}_2$  thin film growth was deposited using  $\text{SiH}_4/\text{N}_2\text{O}$  precursor ratio, with the identifiable peaks of C-H bending doublet at 1870 – 1380  $\text{cm}^{-1}$ , Si-H bending at  $\sim 1200$   $\text{cm}^{-1}$ , Si-O stretching at  $\sim 950$   $\text{cm}^{-1}$ , and Si-O bending at  $\sim 810$   $\text{cm}^{-1}$ . The  $\text{SiN}_x$  thin film growth was deposited using  $\text{SiH}_4/\text{NH}_3$  gases (Figure 3.1). Identifiable peaks include C-H bending at 1870 – 1380  $\text{cm}^{-1}$  and Si-N stretching at 900 – 850  $\text{cm}^{-1}$ . While small trace of the O-H stretching peak was present in the 3700 – 3350  $\text{cm}^{-1}$  region, the direct thin film growth on the pellet did not have prominent hydroxide features.

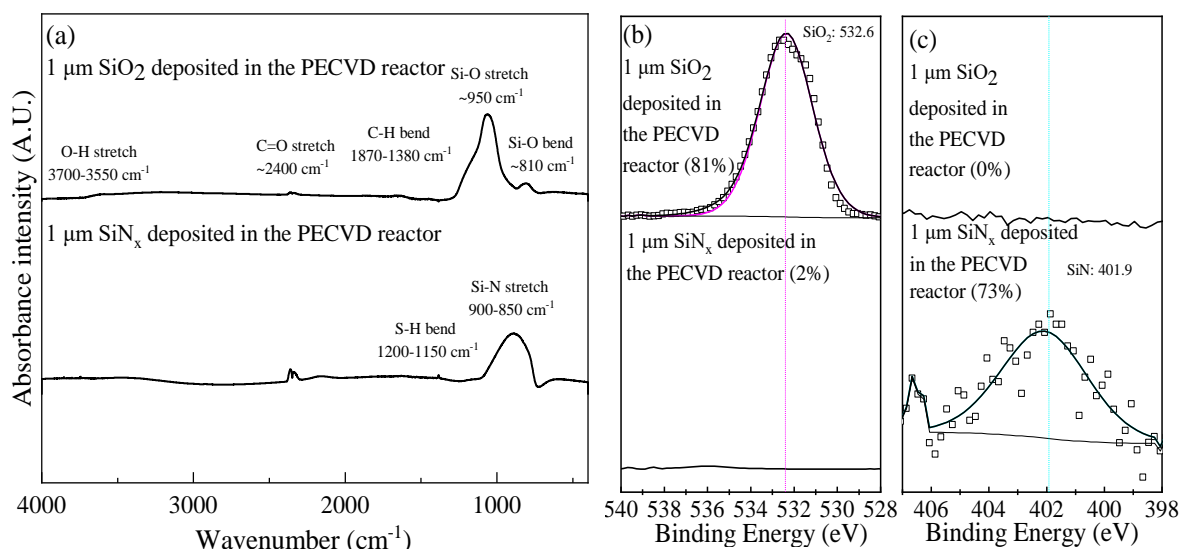


Figure 3.1 (a) Fourier transform infrared absorbance scans of 1 μm SiO<sub>2</sub> and SiN<sub>x</sub> thin film on KBr pellets deposited in the plasma-enhanced chemical vapor deposition reactor. Scans went through signal averaging and KBr background scan subtraction. High-resolution X-ray photoelectron spectroscopy spectra of (b) O 1s and (c) N 1s regions with atomic percent composition labeled.

Following the FTIR absorption scan, the chamber deposited pellets went through XPS scans to analyze the elemental composition on the pellet surface. The silicon dioxide deposited film has 81.4% oxygen with a binding energy peak at 532.6 eV such that the associated atomic composition is bonded to silicon to form SiO<sub>2</sub>. On the other hand, the SiN<sub>x</sub> deposited pellet has 73.4% nitrogen with a binding energy peak at 401.9 eV, which forms a bond with silicon to form SiN<sub>x</sub>.

To simulate silane byproduct formation and accumulation at the PECVD exhaust, multilayer thin films using SiO<sub>2</sub> and SiN<sub>x</sub> were grown alternately on a single KBr pellet (Figure 3.2 (a)). Each scan has been subtracted from the previous layer so that it represents the signature of the newly added layer. The data show that, for silicon dioxide and silicon nitride regions, there is a Si-O stretching peak at 1090 cm<sup>-1</sup> and a Si-O bending peak at 800 cm<sup>-1</sup>. Si-O rocking does not show up due to weak peak intensity and a poor signal-to-noise ratio near the limit of the FTIR detector. Si-H stretching and bending, as well as Si-N stretching, were observed. There is a peak missing for the N-H stretching node at 3350 cm<sup>-1</sup> due to a lack of moisture. The

multilayer deposition above 3  $\mu\text{m}$  induced stress and film delamination of depositions, altering the signal-to-noise ratio and intensity of peaks on the last layer. The multilayer deposition yielded a film thickness that was too large, resulting in delamination. However, this was by design to guarantee a high enough signal-to-noise ratio so the chemical composition of the films could be verified on the KBr pellet. Now that upstream product reference is created, the results of the other experiments were compared with those of the growth experiment to accurately identify features found in these pellets.

### 3.2 *In-situ* Fourier Transform Infrared Experiment

During the growth test in PECVD, the *in-situ* FTIR experiment was taken simultaneously. A single KBr pellet that was placed in the *in-situ* FTIR chamber was analyzed and compared to establish the relationship between upstream and downstream depositions. Both absorbance scans of the chamber and *in-situ* FTIR pellets had minute moisture content. As a result of the thick deposition, the multilayer growth displays absorbance scans with significantly increased peaks, while the *in-situ* FTIR data (Figure 3.2 (b)) displays weaker Si bonded characteristic peaks due to a lack of exposure and a conditional difference originating from its distance from the chamber and nitrogen purging. This displays little to no O-H and Si-OH constituents, dropping the risk of silanol formation in a purged environment. Overall, the *in-situ* FTIR absorbance scan shows less exposure to moisture and organic matter but has the same features as those of the growth experiment with reduced intensities.

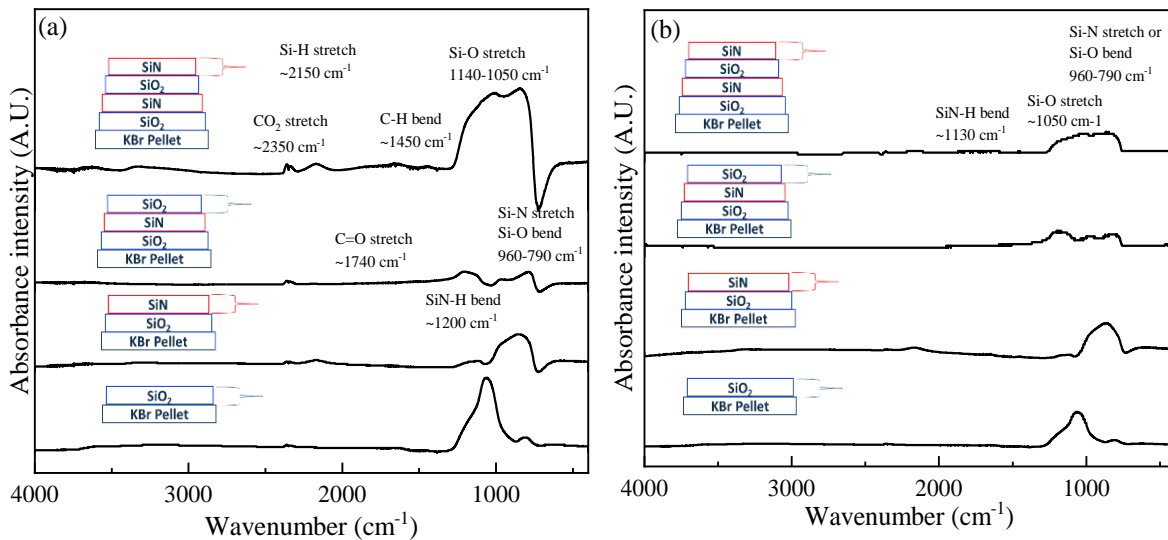


Figure 3.2 (a) Fourier transform infrared (FTIR) absorbance scan of multilayer growth experiment using sequential deposition using SiO<sub>2</sub> and SiN<sub>x</sub> on a KBr pellet. (b) *In-situ* FTIR absorbance scan obtained simultaneously during the multilayer growth. Each layer has signal subtracted from the previous scanned layer to represent the topmost deposits.

The byproduct formation observed in the *in-situ* FTIR chamber shows less accumulation of deposition in the downstream area, which mimics a much more accurate representation of the silane reaction environment. This experiment was able to compare establish real time silicon dioxide and nitride features connected to the downstream area and identify characteristic peak formation such as Si-O stretching at ~1050 cm<sup>-1</sup> and Si-N stretching at ~800 cm<sup>-1</sup>. Thus, *in-situ* FTIR provides real-time changes and is capable of offering kinetics and dynamic changes in a reaction.

### 3.3 Exhaust Monitoring Experiment

KBr pellets that were located in the downstream line of the PECVD tool were extracted monthly as a means of monitoring long-term byproduct accumulation. The process time that each pellet experienced is tabulated in Figure 3.3, b. These pellets were weighed and subtracted from their corresponding initial KBr pellet masses to account for deposition masses. The absolute deposition mass showed an increasing trend from 0.0, 1.1, 1.9, to 2.4 mg (Figure 3.3, (a)). With respect to silane exposure time in hours, the absolute deposition mass shows a trend



of 0.0, 0.16, 0.14, and 0.14 mg. Dividing absolute deposition mass by respective process time associated with each pellet ID, the deposition rate averages out to 0.15 mg/hour. Thus, the majority of the thin film accumulated on the PECVD extracted pellet is attributed to silane exposure.

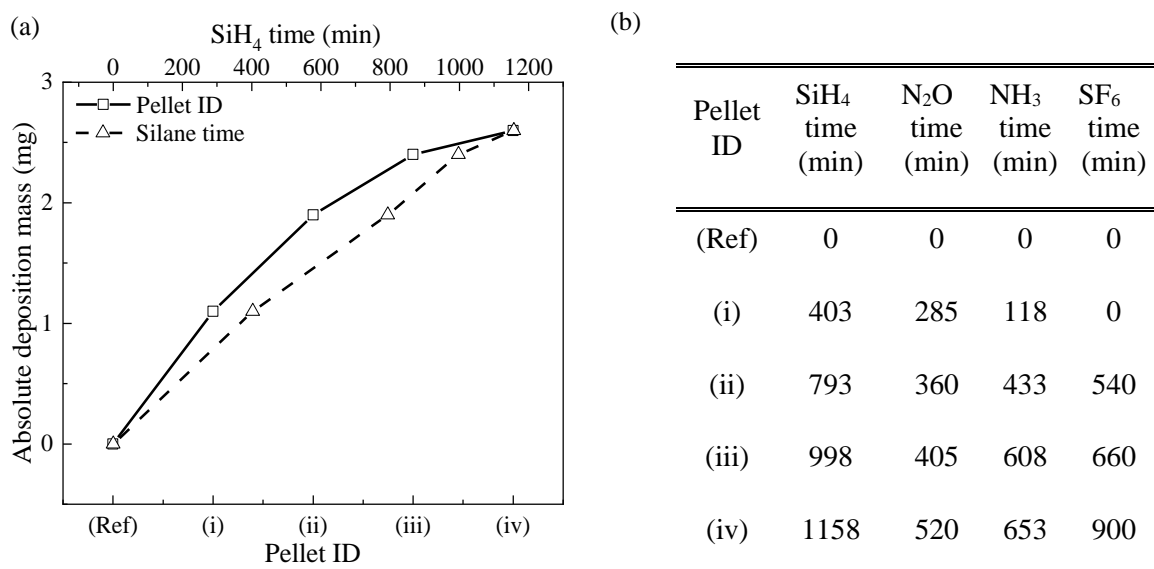


Figure 3.3 (a) Absolute deposition versus pellet ID (bottom x-axis) and silane exposure time (top x-axis) of plasma-enhanced chemical vapor deposition exhaust extracted pellets. Each extracted pellet was subtracted with its original KBr pellet to show only deposition mass. (b) Process logbook tabulated with processing time and precursors. For SiO<sub>2</sub>, SiN<sub>x</sub>, and chemical cleaning, SiH<sub>4</sub>/N<sub>2</sub>O, SiH<sub>4</sub>/NH<sub>3</sub>, and SF<sub>6</sub>/N<sub>2</sub>O ratios were processed, respectively.

These extracted pellets went through FTIR spectroscopy, where signals were averaged, and the corresponding initial KBr pellet signals were subtracted. Absorbance scans of exhaust monitoring experiments of PECVD (Figure 3.4) reveal a consistent pattern in which the absorbance signal increases with the deposition accumulating over time. The integrated peak signals for SiO<sub>2</sub>, SiN<sub>x</sub>, and silanol are observed in all extracts. Significant absorption intensity gains can be seen for O-H (0.08 to 0.12) and Si-OH (0.09 to 0.14) stretching vibrational nodes as more silanol builds up hydroxide constituents.

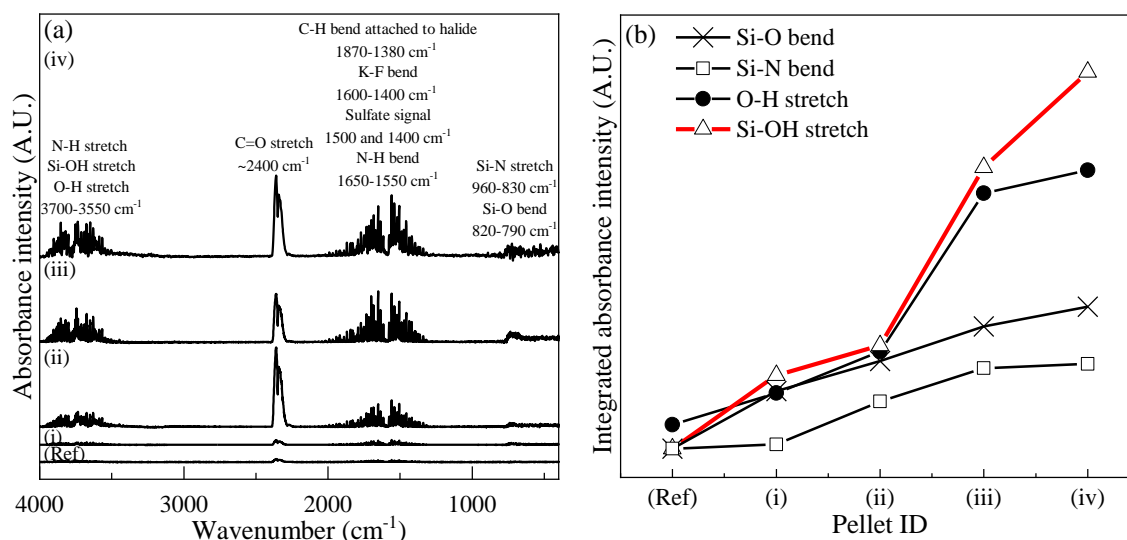


Figure 3.4 (a) Absorbance scans of plasma-enhanced chemical vapor deposition exhaust extracted pellets. All spectra are averaged using five different areas of a pellet and subtracted from the KBr background signals. Extracted pellets were exposed to hours of  $\text{SiH}_4$ ,  $\text{N}_2\text{O}$ ,  $\text{NH}_3$ , and  $\text{SF}_6$ : (i) 7, 5, 2, 0, (ii) 13, 6, 7, 9, and (iii) 17, 7, 10, 11, and (iv) 3, 2, 1, 4. (Ref) As prepared KBr pellet was scanned for reference. (b) Trend of integrated absorbance intensity of Si-O bending  $\sim 1100$  at  $\text{cm}^{-1}$ , Si-N bending  $\sim 870$  at  $\text{cm}^{-1}$ , O-H stretching  $\sim 3701$  at  $\text{cm}^{-1}$ , and Si-OH stretching at  $\sim 3652$   $\text{cm}^{-1}$  regions of each pellet.

Subsequently, these extracted pellets went through XPS scans to identify the elemental composition on the surface. The XPS analyzes the last process each tool experienced before extraction and observes the surface's elemental composition. These scans were calibrated to the advantageous carbon 1s peak at 284.8 eV, and the F, O, K, C, S, Si, and Br elements observed in the survey went through high-resolution scans, while no nitrogen peaks were present (Figure 3.5).

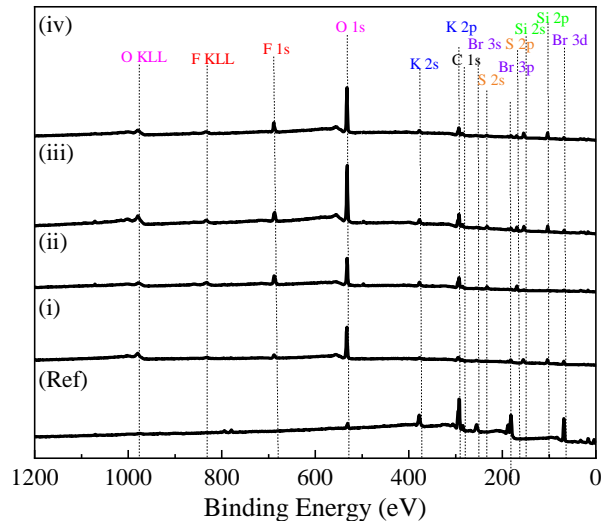


Figure 3.5 X-ray photoelectron spectroscopy survey scans of plasma-enhanced chemical vapor deposition exhaust extracted pellets. Extracted pellets were exposed to (i) 0.5 hour of  $\text{SiH}_4/\text{NH}_3$ , (ii) 3 hours of  $\text{SF}_6$ , (iii) 1.5 hours of  $\text{SiH}_4/\text{N}_2\text{O}$ , and (iv) 2 hours of  $\text{SF}_6$  prior to extraction. (Ref) As prepared KBr pellet was scanned for reference.

For F 1s scans, the peaks consist of both fluorocarbon and potassium fluoride. The concentration nearly doubled from (i) to (ii), which can be attributed to the chemical cleaning process involving  $\text{SF}_6$ . Oxygen 1s scans have distinct silicon dioxide and hydroxide peaks. Given the hygroscopic nature of the pellet, it tends to accumulate hydroxide more readily. The potassium 2p scans contribute to the formation of potassium hydroxide, fluoride, or bromide. The carbon 1s is detected with peaks indicating the presence of C-C, organic, and fluorocarbon bonding. The sulfur 2p scans suggest the possible presence of potassium sulfate. The (ii) atomic composition of sulfur increases as chemical cleaning process time is doubled from the extracted (i) pellet. On the contrary, the silicon 2p scans show a reduction in concentration, suggesting that the chemical cleaning gases have removed silicon compounds from the pellet's surface. The potassium 3d scans have peaks of potassium bromide. Similar to the silicon scans, deposits on the surface reduce the atomic concentration of bromide on the surface, covering our substrate of choice. Notably, chemical cleaning with  $\text{SF}_6$  resulted in the observed F, forming KF or  $\text{C}_x\text{F}_y$  bonds.  $\text{SiO}_2$ ,  $\text{KSO}_4$ , KOH, and C-O made up the O 1s peaks. The  $\text{SiO}_2$  and  $\text{SiN}_x$  features associated with O 1s and N 1s scans are found (Figure 3.6).

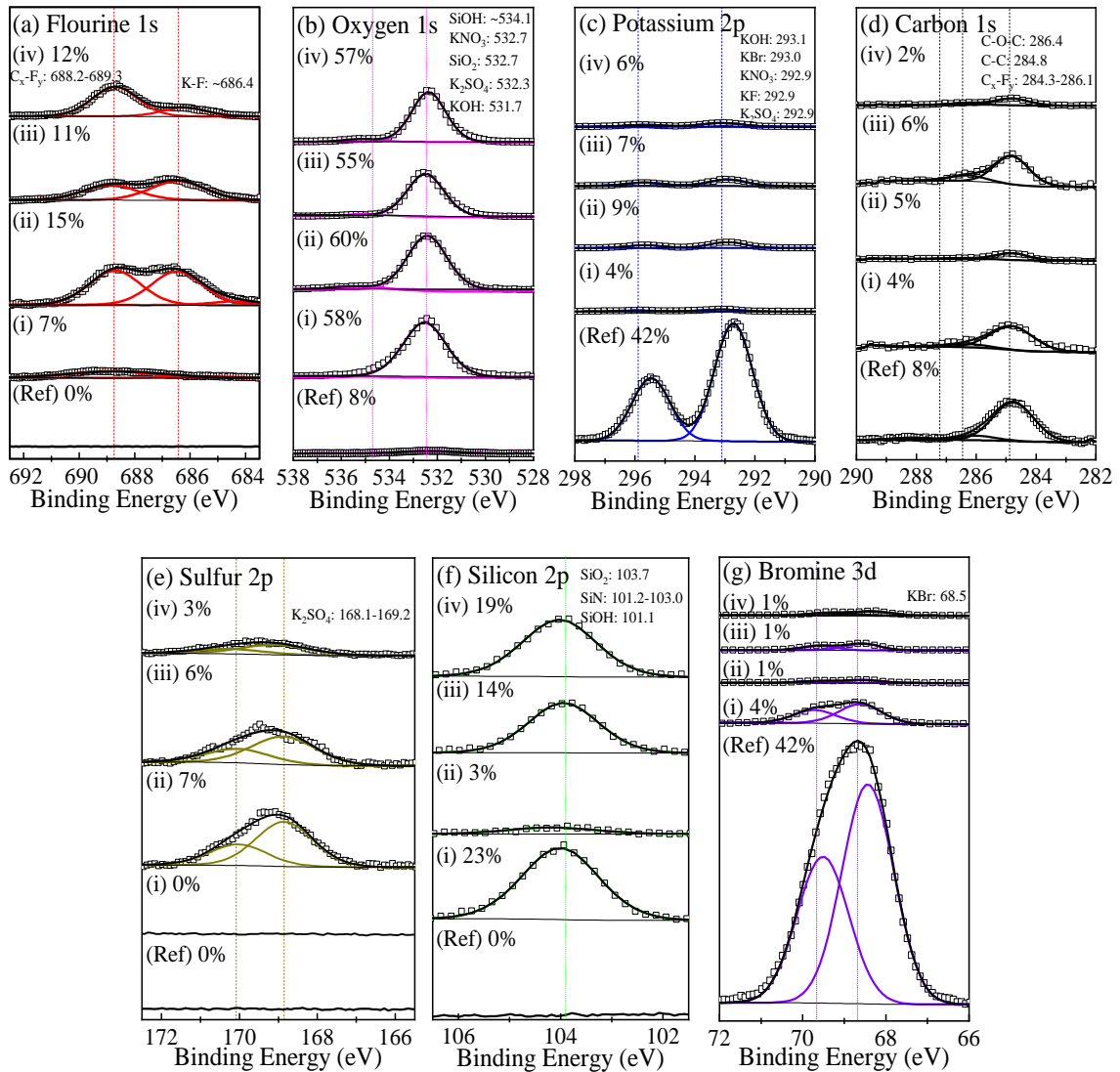


Figure 3.6 High-resolution X-ray photoelectron spectroscopy spectra of (a) F 1s, (b) O 1s, (c) K 2p, (d) C 1s, (e) S 2p, (f) Si 2p, and (g) Br 3d regions of extracted pellets from PECVD exhaust. Extracted pellets were exposed to (i) 0.5 hour of  $SiH_4/NH_3$ , (ii) 3 hours of  $SF_6$ , (iii) 1.5 hours of  $SiH_4/N_2O$ , and (iv) 2 hours of  $SF_6$  prior to extraction. (Ref) As prepared KBr pellet was scanned for reference. Atomic compositions and possible compounds associated with the binding energy peak are labeled.

The atomic composition of the pellets extracted from the PECVD exhaust were determined by using the relative sensitive factor (RSF) and fitted peak areas from the CASA XPS software. This example seeks to provide a detailed breakdown of relative elemental composition and concentrations inside the 10 nm depth surface of the extracted pellet, providing insights into the material properties produced in the downstream line. The overall atomic percent (At%) was determined using the parameters tabulated in Table 2.5.

Observing the atomic compositional trend of the fluorine plot, the fluorine concentration largely depends on how recent the chemical cleaning process was before the extraction as seen in (ii) and (iv); this also results in the removal of oxygen bonded products and adds sulfur concentration. The oxygen atomic composition trend increases up to (iii) as  $\text{SiO}_2$  and silanol are the main deposits found in the extracts. The sulfur atomic composition builds up and increases by forming bonds with potassium and oxygen over time. The trend of bromine can be explained in two possible ways: a decrease in bromine from sulfur in the form of sulfate, replacing the bond with potassium bromide, and an increase in bromine from fluorine, removing the surface deposition on top of bromine.

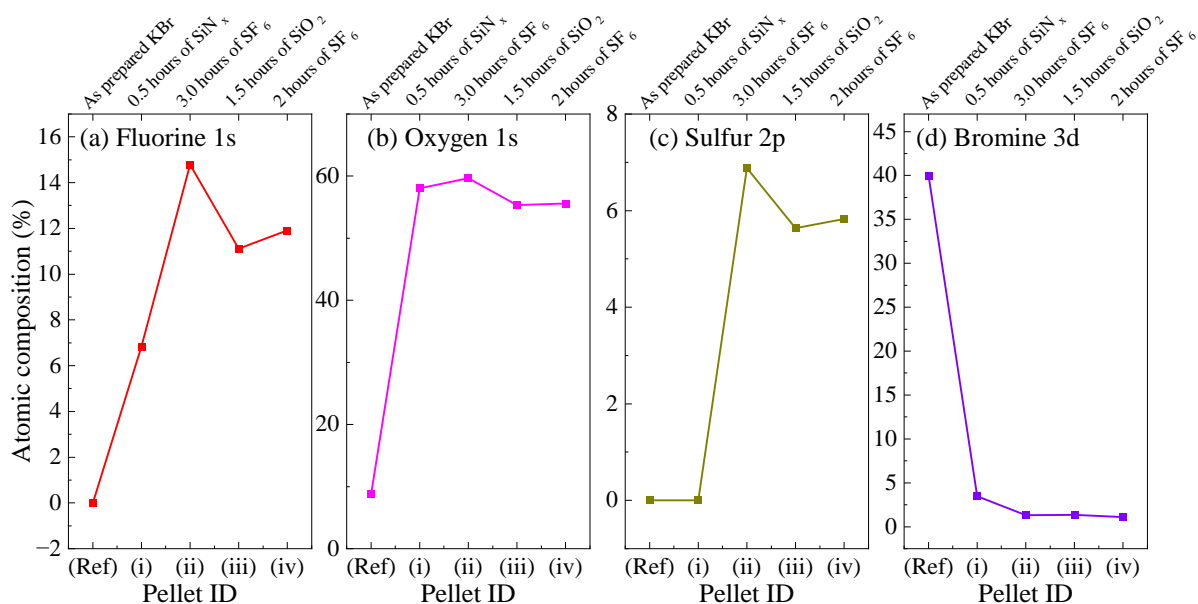


Figure 3.7 Pellet ID versus atomic composition graphs of selected electronegative elements. Atomic compositional trends are shown for (a) F 1s, (b) O 1s, (c) S 2p, and (d) Br 3d. Top x-axis is extracted pellets that were exposed to (i) 0.5 hour of  $\text{SiH}_4/\text{NH}_3$ , (ii) 3 hours of  $\text{SF}_6$ , (iii) 1.5 hours of  $\text{SiH}_4/\text{N}_2\text{O}$ , and (iv) 2.0 hours of  $\text{SF}_6$  prior to extraction. (Ref) As prepared KBr pellet was scanned for reference. The bottom x-axis pellet ID associated with the element atomic composition.

### 3.4 Summary

This chapter had three different experiments conducted as part of the PECVD inquiry into silane chemistry, which provided insight into a number of elements of the material's behavior and byproduct generations. In the FTIR analysis, a clear trend emerged as the absorbance intensity exhibited a notable increase corresponding to the growing mass of the deposited film (Figures 3.3 and 3.4). The silanol or Si-OH absorbance peak integrated intensity increased as the deposited mass increased from 1.1 mg to 2.4 mg, resulting in a deposition rate of 0.15 mg/hour of silane exposure. The FTIR spectra demonstrated a direct correlation between the deposited film mass and the absorbance intensity, indicating a proportional relationship. This observation suggests that as the film mass increases, there is a concurrent rise in the absorbance signals detected by FTIR. The increase in characteristic compositional peaks of O 1s and Si 2p suggests silanol group buildup on the pellet surface. This raises concern about raising the safety risk once the byproduct accumulates on the surface. This byproduct not only acts as a reactive deposit but also as a catalytic surface for reactive species to interact with, underscoring the importance of rigorous monitoring and control throughout the deposition process.

When exposed to diverse reactants or conditions, silanol can participate in a variety of energetic reactions, potentially increasing the risk in the manufacturing environment. Hydrolysis reactions like  $\text{Si(OH)}_4(\text{g}) \rightarrow \text{H}_2\text{SiO}_3(\text{s}) + \text{H}_2\text{O}(\text{g})$  are a typical process involving silanol in which the Si-OH bond reacts with  $\text{H}_2\text{O}$  to form siloxane bonds and release hydrogen gas. This reaction not only changes the chemical composition of silanol but also generates flammable hydrogen gas that has a fire or explosion risk in the presence of an ignition source. The Gibbs free energy change for this hydrolysis reaction has a negative value of -1093 kJ at 298 K, indicating its spontaneity under typical conditions. Silanol pyrolysis reactions like  $\text{Si}(\text{s}) + 2\text{H}_2(\text{g}) + 2\text{O}_2(\text{g}) \rightarrow \text{Si(OH)}_4(\text{g})$  and  $\text{Si(OH)}_4(\text{g}) \rightarrow \text{H}_2\text{SiO}_3(\text{s}) + \text{H}_2\text{O}(\text{g})$  yield associated

Gibb's free energy values of -1317 kJ and -1093 kJ, respectively. Meanwhile, condensation reactions of silanol produce siloxanes and water as byproducts, also releasing heat energy. These exothermic reactions can lead to thermal runaway reactions. Additionally, silanol interacts with ammonia and nitrous oxide, both of which are commonly found in manufacturing environments. Amine-substituted siloxanes and nitrosiloxanes, for example, are particularly hazardous due to their poisonous or reactive properties. Overall, the energetic reactions involving silanols highlight the importance of understanding and managing these chemical processes in semiconductor production to safeguard the safety of workers and equipment.

Another concern of EH&S and financial concerns was brought up when fluorine and sulfur byproducts from PECVD accumulate throughout the semiconductor production process. Regulation adherence is required because the production of perfluorinated compounds (PFCs), especially those containing fluorine, is a contributing factor to global warming potential (GWP) and greenhouse gas (GHG) emissions (SEMI, 2020). Because fluorine and sulfur chemicals pose health dangers to workers, ensuring their safety is of utmost importance. Adherence to safety regulations is essential for safeguarding people in these settings. Achieving a balance between safety and economic considerations in semiconductor manufacturing entails investigating alternate deposition technologies or optimizing current procedures while recognizing the interdependent issues of worker safety, environmental responsibility, and financial feasibility.

## CHAPTER 4: MONITORING AND ANALYSIS OF ALD SYSTEM

This chapter had two different experiments conducted in an atomic layer deposition tool, utilizing cycles of  $\text{Al}(\text{CH}_3)_3/\text{H}_2\text{O}$  and  $\text{Hf}(\text{NMe}_2)_4/\text{H}_2\text{O}$  for  $\text{Al}_2\text{O}_3$  and  $\text{HfO}_2$  deposition. Due to the physical space limitations of the deposition tool setup, growth and exhaust monitoring experiments were done to understand the effect the upstream chamber reactions have on its downstream line. *Ex-situ* Fourier transformation infrared spectroscopy analyses of thin film deposited in the reactor showed metal oxide absorbance peaks of Al-O bending and Hf-O bending in the  $800 - 700 \text{ cm}^{-1}$  range. The exhaust monitoring experiment observed the accumulation of reaction chemistry byproducts in the downstream area on a monthly basis. The absolute mass of deposits on each extracted pellet increased over time as precursors and byproducts collected on the pellets. As processing time for  $\text{Al}(\text{CH}_3)_3$ ,  $\text{Hf}(\text{NMe}_2)_4$ , and  $\text{H}_2\text{O}$  increased, characteristic vibrational peaks amplified: Hf-OH stretching at  $\sim 3650 \text{ cm}^{-1}$ , and Al-OH stretching at  $\sim 3784 \text{ cm}^{-1}$  disclosed features of metal hydroxide formation. The X-ray photoelectron spectroscopy analyses show that the atomic composition and relative atomic concentration of oxygen 1s and hafnium 4f binding energy peaks increase as processing time increases. The presence of fluorine byproducts is identified from exhaust interconnected tools with fluorocarbon, trifluoro methane, and sulfur hexafluoride. Heavy metal reaction byproducts are difficult to accumulate and deposit evenly, but the chemical composition of high metal hydroxide reveals highly exothermic reactions. Using the point-of-use abatement system and cleaning the exhaust with isolation need to be controlled to prevent fluorine and water vapor from reacting with the byproducts.



#### 4.1 Growth Experiment in ALD Chamber

For the ALD growth experiment, aluminum oxide and hafnium oxide thin films were produced directly on potassium bromide pellets, using 100 precursor cycles for each oxide. The desired thickness for Al<sub>2</sub>O<sub>3</sub> and HfO<sub>2</sub> thin films was grown using 100 cycles of trimethyl aluminum (TMA)/H<sub>2</sub>O and Hf(NMe<sub>2</sub>)<sub>4</sub>/H<sub>2</sub>O, respectively. The direct growth of thin films on KBr substrates allows for the characterization of the properties of these oxide films using *ex-situ* analysis. Using these directly chamber grown metallic oxides on KBr pellets, the absorbance features of Al<sub>2</sub>O<sub>3</sub> and HfO<sub>2</sub> thin films typically exhibit characteristic peaks associated with the molecular vibrations of the metal oxides. For aluminum oxide, common absorption peaks include a sharp and intense peak near 700 cm<sup>-1</sup>, which corresponds to the Al-O stretching modes. Additionally, peaks in the range of 800 – 1100 cm<sup>-1</sup> may indicate Al-OH bending vibrations or other Al-O-related modes. Hafnium oxide, on the other hand, generally shows characteristically less intense and broader peaks in the range of 700 cm<sup>-1</sup>, associated with Hf-O stretching vibrations. Unlike the PECVD chamber deposited thin film, the inherent ALD cyclic process reacts organometallic precursors with of water, providing functional O-H stretching peaks in all absorbance spectra. These FTIR features are essential for identifying and confirming the presence of aluminum and hafnium oxides, aiding in the structural characterization of thin films. With the given setup, both thin film Al<sub>2</sub>O<sub>3</sub> and HfO<sub>2</sub> deposited directly on KBr pellets in the chamber showed characteristic peak intensities near 700 cm<sup>-1</sup> regions (Figure 4.1).

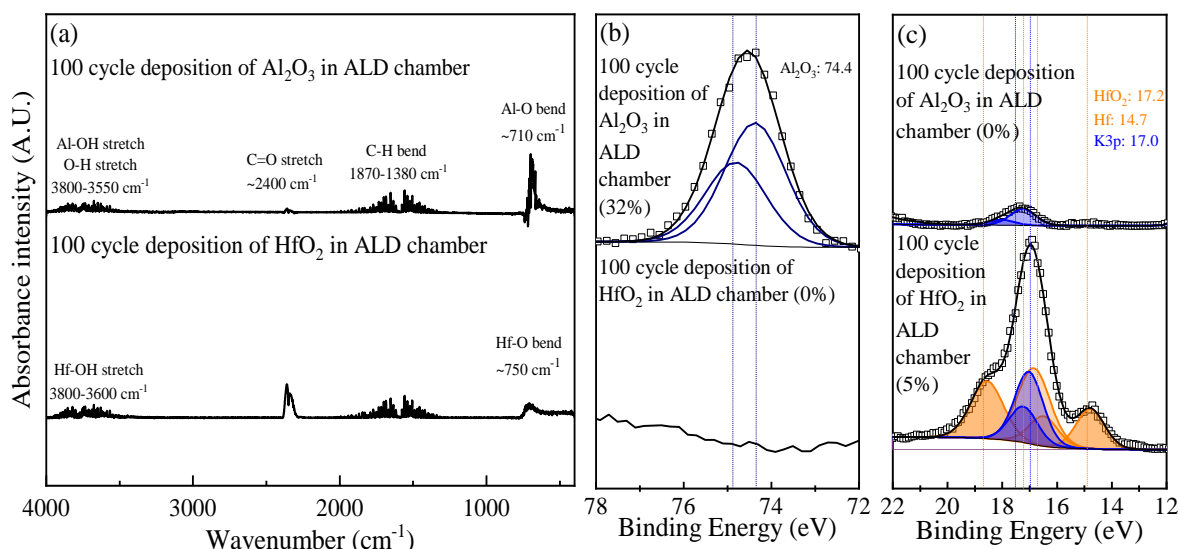
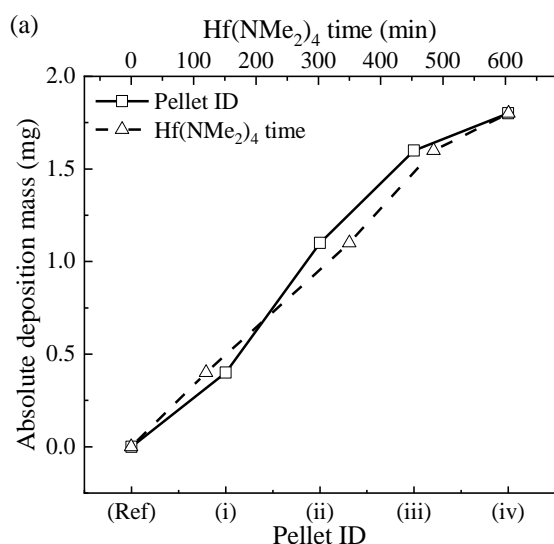


Figure 4.1 (a) Fourier transform infrared (FTIR) absorbance scans of 100 cycles growth of Al<sub>2</sub>O<sub>3</sub> and (ii) HfO<sub>2</sub> in atomic layer deposition chamber on KBr pellets. Scans went through signal averaging and KBr background scan subtraction. High-resolution X-ray photoelectron spectroscopy spectra of (b) Al 2p and (c) Hf 4f regions with atomic percent composition are labeled.

The XPS scans of aluminum and hafnium oxide thin films deposited on KBr pellets typically reveal distinctive peaks corresponding to the elemental composition of the oxides. For aluminum oxide, the XPS spectrum exhibited peaks associated with the Al 2p and O 1s regions. The Al 2p peak (Figure 4.1 (a)) showed 32.0% in atomic composition that forms bonds with oxygen with the oxidation state of aluminum at a 2:3 ratio. Similarly, in the case of hafnium oxide, the XPS spectra showed Hf 4f and O 1s peaks that are key indicators of hafnium oxidation states and the oxygen content in the film. The Hf 4f (Figure 4.1 (b)) had a low 4.7% atomic composition, implying that it is difficult for hafnium to form oxides on a KBr substrate. Analyzing the binding energies and compositional results can offer insights into the chemical composition, bonding environments, and oxidation states of aluminum and hafnium oxides on the KBr pellets. This information is crucial for characterizing the properties of thin films in various applications.

## 4.2 Exhaust Monitoring Experiment

The correlation between upstream and downstream of the ALD tool was assessed by comparing its downstream area deposit with chamber grown results. The KBr pellets that sat in the ALD downstream line were extracted monthly. These monthly extracted pellets' process time and precursor usage logbook experiences in the ALD exhaust are tabulated in Figure 4.2, b. The deposition masses were calculated by subtracting the initially measured KBr pellets from their corresponding extracted pellets. The absolute deposition mass trend increases from 0.0, 0.4, 1.1, and 1.6 mg and displays a gain in deposits on the pellets when more processing byproducts introduced. The deposition mass directly correlates with hafnium precursor usage time. The deposition rate of 0.20, 0.19, and 0.20 averages to 0.20 mg/hour of  $\text{Hf}(\text{NMe}_2)_4$  exposure and show similar trend of deposition mass gain associated with pellet ID. While the  $\text{Al}(\text{CH}_3)_3$  has been the major precursor processed in the tool, the deposition rate does not demonstrate absolute deposition rate.



Pellet ID	$\text{Al}(\text{CH}_3)_3$ time (min)	$\text{Hf}(\text{NMe}_2)_4$ time (min)	$\text{H}_2\text{O}$ time (min)
(Ref)	0	0	0
(i)	735	120	855
(ii)	7090	350	7440
(iii)	7640	485	8125
(iv)	7880	605	8485

Figure 4.2 (a) Absolute deposition versus pellet ID (bottom x-axis) and silane exposure time (top x-axis) of atomic layer deposition exhaust extracted pellets. Each extracted pellet was subtracted with its original KBr pellet to show only deposition mass. (b) Process logbook tabulated with process time and organometallic precursors. For  $\text{Al}_2\text{O}_3$  and  $\text{HfO}_2$ ,  $\text{Al}(\text{CH}_3)_3/\text{H}_2\text{O}$  and  $\text{Hf}(\text{NMe}_2)_4/\text{H}_2\text{O}$  cycles were processed, respectively.

It is important to note that aluminum oxide bending is difficult to identify, as the most prominent symmetric peak features of  $\text{Al}_2\text{O}_3$  lies at the limit of the detector range of  $400\text{ cm}^{-1}$ . The same can be said for hafnium oxide because its metallic vibrational nodes also exist in low wavenumber regions where sensitivity is low, and the signal-to-noise ratio is poor. While the detector resolution cannot differentiate these two peaks, these exhaust extracts have coherent metal (M) oxide bending features in  $700 - 800\text{ cm}^{-1}$  and correspond to a combination of both Al-O and Hf-O bending peaks (Figure 4.3 (a)). While the most distinguishable vibrational nodes are metal oxides, other integrated absorbance peaks in the forms of M-OH (both Hf-OH and Al-OH) showed metallic hydroxide bonds accumulating over time in  $3800 - 3650\text{ cm}^{-1}$  range.

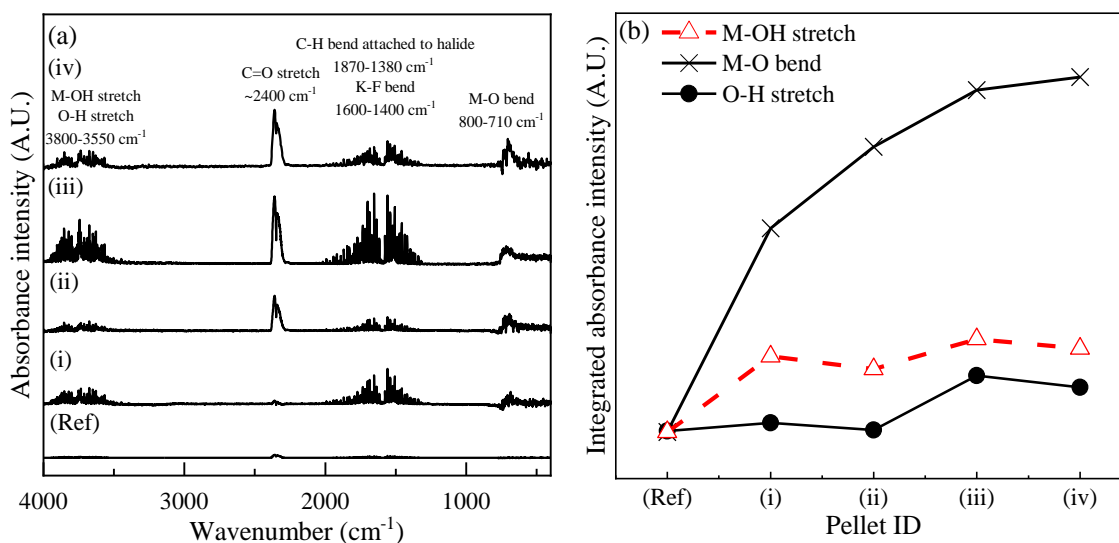


Figure 4.3 (a) Absorbance scans of atomic layer deposition exhaust extracted pellets. All spectra are averaged using five different areas of a pellet and subtracted from the KBr background signals. Extracted pellets were exposed to hours of  $\text{Al}(\text{CH}_3)_3$ ,  $\text{Hf}(\text{NMe}_2)_4$ , and  $\text{H}_2\text{O}$ : (i) 12, 2, 14, (ii) 118, 6, 124, (iii) 127, 8, 135, and (iv) 4, 2, 6. (Ref) As prepared KBr pellet was scanned for reference. (b) Trend of integrated absorbance intensity of M-O bending at  $800-710\text{ cm}^{-1}$ , O-H stretching at  $\sim 3700\text{ cm}^{-1}$ , M-OH stretching at  $3800 - 3650\text{ cm}^{-1}$  of each pellet.

After the FTIR scans, the extracted pellets were followed by XPS scans and were calibrated with advantageous C 1s peak. The survey scan scans indicate the presence of F, O, K, C, Br, and Hf elements (Figure 4.4). Unlike the chamber grown  $\text{Al}_2\text{O}_3$  thin film, the XPS

scans did not show any presence of Al 2p peaks but F 1s peaks were observed.

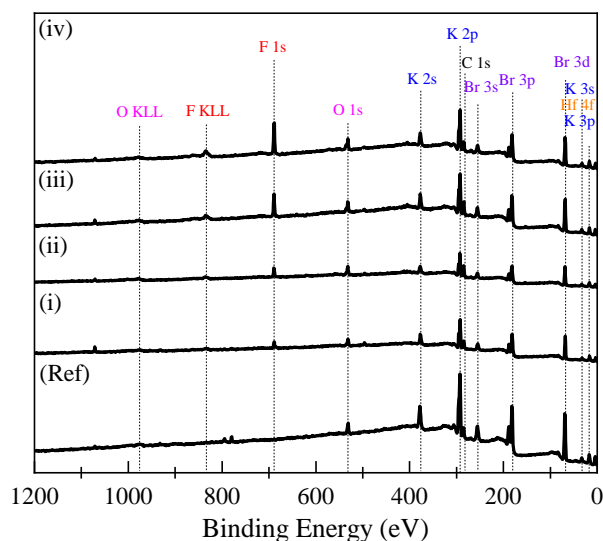


Figure 4.4 X-ray photoelectron spectroscopy survey scans of atomic layer deposition exhaust extracted pellets. Extracted pellets were exposed to (i) 3 hours of  $\text{Hf}(\text{NMe}_2)_4/\text{H}_2\text{O}$ , (ii) 3 hours of  $\text{Al}(\text{CH}_3)_3/\text{H}_2\text{O}$ , (iii) 0.5 hours of  $\text{Al}(\text{CH}_3)_3/\text{H}_2\text{O}$ , and (iv) 2 hours of  $\text{Hf}(\text{NMe}_2)_4/\text{H}_2\text{O}$  prior to extraction. (Ref) As prepared KBr pellet was scanned for reference.

For F 1s scans, the concentration increases and associated binding energy comes from fluorocarbon, potassium bromide, or oxyfluoride compounds. The ALD extract samples had exposure to the interconnected oxide or rapid ion etcher exhaust line that utilized fluorocarbon,  $\text{CHF}_3$ , and  $\text{SF}_6$  precursors. In the O 1s scans, the presence of hafnium oxide, potassium oxide, and oxyfluoride can be found. The Hf 4f scans show where hafnium oxide, K 3p, and hf bonds are located. As the hafnium scan has multicomponent overlapping at detector limit, the hafnium concentration may be less than the amount integrated. Since the source of fluorine is not provided by the ALD tool, its concentration could depend on the use of  $\text{C}_x\text{F}_y$ ,  $\text{CHF}_3$ , and  $\text{SF}_6$  from other downstream interconnected tools.  $\text{O}_x\text{F}_y$  or  $\text{HfO}_2$  are all visible in the O 1s region.  $\text{Al}_2\text{O}_3$  features are not identified in its binding energy region and are only seen in the thin film grown pellet placed in the chamber, and  $\text{HfO}_2$  has a multicomponent peak possibly from Hf, S, and K.

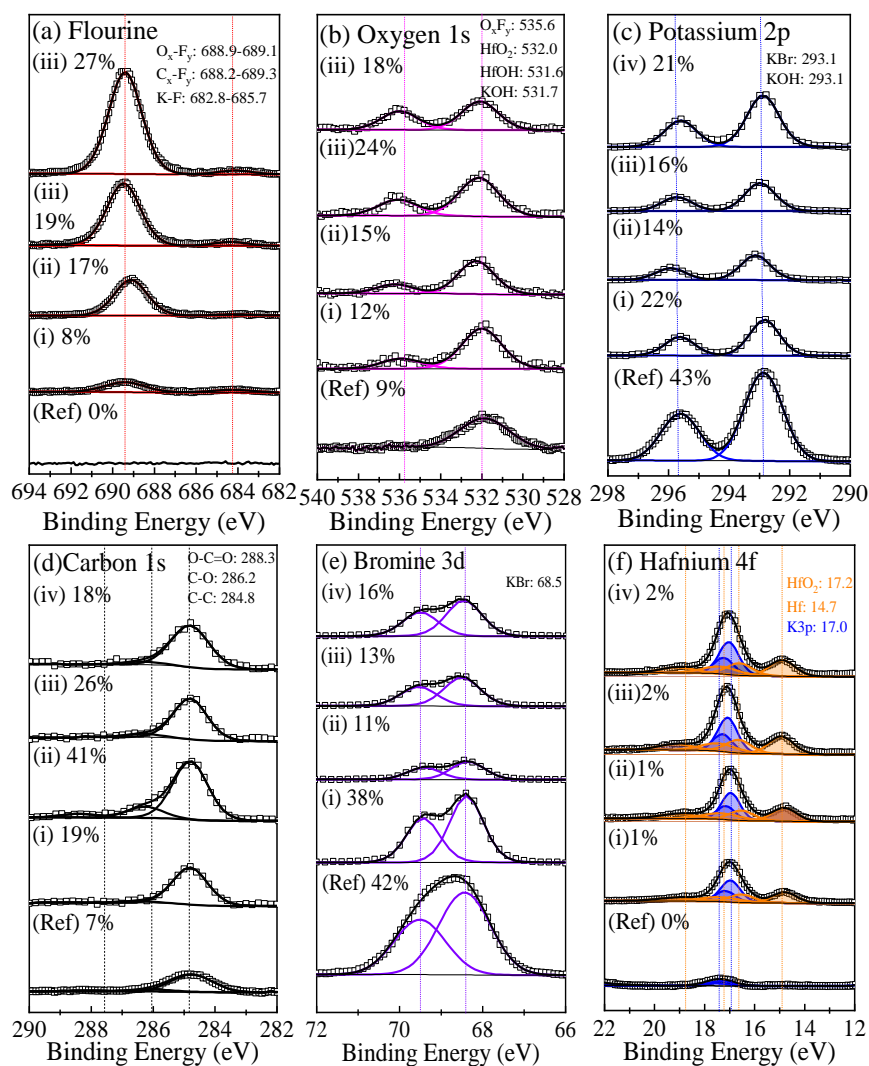


Figure 4.5 High-resolution X-ray photoelectron spectroscopy spectra of (a) F 1s, (b) O 1s, (c) K 2p, (d) C 1s, (e) Br 3d, and (f) Hf 4f regions of extracted pellets from atomic layer deposition exhaust. Extracted pellets were exposed (i) 3 hours of  $\text{Hf}(\text{NMe}_2)_4/\text{H}_2\text{O}$ , (ii) 3 hours of  $\text{Al}(\text{CH}_3)_3/\text{H}_2\text{O}$ , (iii) 0.5 hours of  $\text{Al}(\text{CH}_3)_3/\text{H}_2$ , and (iv) 2 hours of  $\text{Hf}(\text{NMe}_2)_4/\text{H}_2\text{O}$  prior to extraction. (Ref) As prepared KBr pellet was scanned for reference. Atomic compositions and possible compounds associated with the binding energy peak are labeled.

The atomic compositional trend of the ALD exhaust extracts shows an increase in fluorine, as the latest process of the interconnected reactive-ion etcher tool was 3 hours of  $\text{C}_4\text{F}_8$  4 days before extraction. In the atomic compositional trend (Figure 4.6 (b)), the oxygen concentration increased as more oxide deposits accumulated on the hygroscopic substrate. The hafnium concentration had increased, but the latest process of (ii) pellet was aluminum oxide, which did not appear in survey or detailed XPS scans. From a processing standpoint, one could

speculate that the increase in its concentration may be due to the doubling of the overall hafnium oxide deposition process time since (i) pellet. The bromine concentration decreases significantly, near 30%, as other deposits cover up the pellet surface.

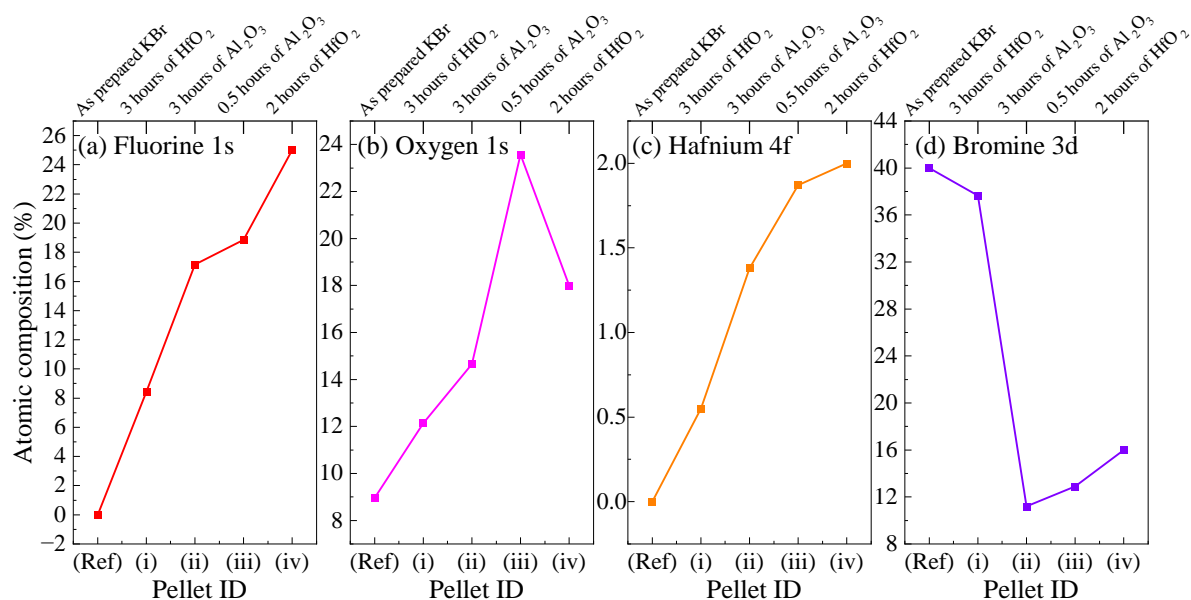


Figure 4.6 Pellet type versus atomic composition graphs of selected elements. Atomic compositional trends are shown for (a) F1s, (b) O1s, (c) Hf 4f, and (d) Br 3d. Top x-axis is extracted pellets that were exposed to (i) 3 hours of Hf(NMe<sub>2</sub>)<sub>4</sub>/H<sub>2</sub>O, (ii) 3 hours of Al(CH<sub>3</sub>)<sub>3</sub>/H<sub>2</sub>O, (iii) 0.5 hours of Al(CH<sub>3</sub>)<sub>3</sub>/H<sub>2</sub>O, and (iv) 2 hours of Hf(NMe<sub>2</sub>)<sub>4</sub>/H<sub>2</sub>O prior to extraction. (Ref) As prepared KBr pellet was scanned for reference. The bottom x-axis is types of pellets associated with the composition.

### 4.3 Summary

The chamber growth experiment was able to identify characteristic peaks of FTIR and XPS for organometallic depositing precursors. Where the Al<sub>2</sub>O<sub>3</sub> had signature Al-OH and Al-O at 3784 cm<sup>-1</sup> and ~710 cm<sup>-1</sup>, respectively, the HfO<sub>2</sub> had similar hydroxide and oxide peaks at 3650 cm<sup>-1</sup> and ~750 cm<sup>-1</sup>. The atomic compositions of these chamber grown thin films had an Al 2p binding energy of 74.4 eV for Al<sub>2</sub>O<sub>3</sub> and an Hf 4f binding energy of 17.2 eV for HfO<sub>2</sub>. The ALD exhaust extracted pellets experienced various processing times from Al(CH<sub>3</sub>)<sub>3</sub>, Hf(NMe<sub>2</sub>)<sub>4</sub>, and H<sub>2</sub>O. The resulting FTIR features had signature M-O and M-OH peaks at 3800

– 3650  $\text{cm}^{-1}$  and 800 – 710  $\text{cm}^{-1}$ , respectively. Both metal oxide and hydroxide features were indistinguishable, but absorbance intensities amplified with increased exposure time. The increase in metal hydroxide integrated peaks implies an increase in exothermic reactions in the downstream area to form these particular substances on the pellet. The ALD exhaust extracted pellets show an accumulation and increase in deposition mass along with their absorbance intensities. The extracted pellet accumulated an absolute deposition mass of 1.6 mg with an average of 0.20 mg/hour of  $\text{Hf}(\text{NMe}_2)_4$  exposure. Given that the XPS scans did not contain  $\text{Al}(\text{CH}_3)_3$  byproducts, hafnium oxide and hydroxide have lower vapor pressures at a given temperature than aluminum byproducts, allowing deposits to form and accumulate in the downstream line. As an outcome, this deposition rate reflects a direct relationship between deposition mass gain and exposure time to hafnium precursors.

Energetic reactions from the use of hafnium-based hydroxides in semiconductor manufacturing processes may present numerous hazards if not properly controlled. Byproducts are formed during hydrolysis, where Hf-OH bonds react with  $\text{H}_2\text{O}$  to produce hafnium oxide, water, and hydrogen gas. This process can be represented by the reaction:  $\text{Hf}(\text{NMe}_2)_4(\text{g}) + 4\text{H}_2\text{O}(\text{g}) \rightarrow \text{Hf}(\text{OH})_4(\text{s}) + 4\text{NMe}_2\text{H}(\text{g})$ . This reaction produces hydrogen gas that poses a significant fire or explosion risk, particularly in the presence of an ignition source. Additionally, the reaction is exothermic, further increasing the accident-prone nature of the environment. To mitigate these risks, the implementation of best-known methods is essential, requiring effective handling, storage, and disposal practices. This includes the utilization of appropriate personal protective equipment, ensuring adequate ventilation, and taking steps to prevent chemical reactions and environmental contamination. Moreover, understanding the pathways leading to the formation of aluminum-based compounds such as aluminum hydroxide and aluminum oxycarbide is critical for managing hazards in semiconductor manufacturing processes. For instance, aluminum hydroxide can be formed through reactions such as:  $\text{Al}(\text{OH})_3(\text{s}) \rightarrow$



$\text{AlO}(\text{OH})(\text{s}) + \text{H}_2\text{O}(\text{g})$  with a Gibbs free energy value of -924 kJ at 298 K. Therefore, a comprehensive understanding of the hazards associated with metal hydroxides and adherence to safety standards are imperative for maintaining a secure working environment and preventing accidents or incidents in industrial operations.

With the high atomic percent of fluorine, the possibility of other exhaust lines contributing to the surface composition must be considered. Whenever the ALD is not running, the pellet may experience exhaust byproduct flow from the downstream connected tools. The current laboratory ALD exhaust line setup is connected to three different tools that use  $\text{C}_3\text{F}_8$ ,  $\text{C}_4\text{F}_8$ ,  $\text{CHF}_3$ , and  $\text{SF}_6$  precursors. From this connection, possible sulfur in the form of S 3s peak composition may be contributing to the 2% of hafnium. This may explain why the hafnium peak is difficult to find in the IR spectrum.

Significant safety risks arise from the accumulation of fluorine and heavy metal oxides in industrial operations, especially in the manufacture of semiconductors. Because of their recognized toxicity, heavy metal oxides can pose serious health concerns to employees if not managed appropriately. Fluorine is a highly reactive and poisonous element that can also lead to safety risks. Severe safety precautions must be taken when these materials build up in processing facilities or equipment to avoid exposure and possible health problems. To protect worker health and the environment, mitigating these safety risks entails putting in place efficient ventilation systems, following safety rules, and using appropriate handling techniques.

## CHAPTER 5: SUMMARY

This study examined silane and trimethyl aluminum chemistries from respective plasma-enhanced chemical vapor deposition (PECVD) and atomic layer deposition (ALD) tools. With the use of Fourier-Transform infrared spectroscopy (FTIR) and of X-ray photoelectron spectroscopy (XPS), the study sought to determine compositions of the experimental byproduct formation and accumulation that were taking place in the downstream lines of these instruments. As a consequence of combining PECVD and ALD with analytical methodologies, there is a better understanding of byproduct formation and accumulation to contribute to mitigating safety problems in the downstream areas of these deposition technologies.

The major byproduct found in the exhaust of the PECVD was silanol, which contributed to an unstable energetic environment. Three separate studies were carried out within the framework of the PECVD experiments investigating the chemistry of silanes. The growth experiment was able to identify functional peaks and composition binding energies of oxide, nitride, and hydroxide vibrational nodes of silicon that were later used to label deposits in both *in-situ* FTIR and exhaust monitoring experiments. The real-time absorption scanned deposits in the exhaust showed less intensified peaks than those directly grown in the chamber, indicating a difference in temperature at the exhaust has silanol byproduct deposits that might react with unused precursors. The exhaust monitoring study, in particular, showed a clear trend: integrated absorbance peak intensities increased significantly in parallel with the increasing use of precursors and tool processing time. The Si-OH stretching near the  $3652\text{ cm}^{-1}$  region is associated with silanol absorbance peaks, and the concentration increased steadily as the deposition accumulated on the extracted pellets. The atomic composition trend of silanol shows an increase in both O 1s and Si 2p at 534 eV and 101 eV, respectively. These associations imply that there is a buildup of reactive species in downstream areas that gives rise to potential

hazards. Both analyses indicate silanol buildup in the exhaust line that requires caution and cleaning to prevent accidents.

The ALD experiment analysis provided insights into metallic hydroxide formation and accumulation in the tool downstream lines. The growth experiment was able to identify upstream aluminum and hafnium oxide functional peaks and compositional binding energies through cycles of  $\text{Al}(\text{CH}_3)_3/\text{H}_2\text{O}$  and  $\text{Hf}(\text{NMe}_2)_4/\text{H}_2\text{O}$  deposition. The exhaust monitoring experiment demonstrated an accumulation of byproduct deposition associated with metal hydroxide signals in the  $3650 - 3800$  and  $700 - 800 \text{ cm}^{-1}$  regions. The rising XPS trends in oxygen 1s at 532 eV and hafnium 4f at 17 eV atomic compositions point to the proportional relationship of metal hydroxides buildup on the surface of the exhaust lines with tool processing time. These pellets' FTIR scans show a corresponding increase in stretching peaks linked to both hafnium and aluminum hydroxides, implying highly reactive and exothermic reactions could occur given unreacted and pyrophoric trimethyl aluminum exposure. This accumulation of deposits underscores the significance of monitoring and managing byproduct generation in semiconductor manufacturing processes, particularly in protracted processing situations, to maintain operational safety and product quality.

There are broader environmental ramifications to the examination of silanol and metal hydroxide byproduct generation and accumulation in both investigations. Sulfur and fluorine byproducts may indicate the release of greenhouse gases, which increases the possibility of global warming (GWP). Concerns regarding the effects on the environment are also raised by the production of heavy metal oxides. Additionally, the weight increase that was seen in the samples' deposition tool exhausts suggests that materials have accumulated over time. This buildup and the presence of potentially dangerous byproducts may cause a localized hotspot to form in the exhaust lines, which might result in an uncontrolled environment that is susceptible to energetic reactions. These results highlight the need for addressing worker safety problems

as well as putting policies in place to reduce environmental impact and alleviate the environmental footprint throughout semiconductor manufacturing processes.

## Appendix

### A1. Plasma-enhanced chemical vapor deposition (PECVD) standard operation procedures

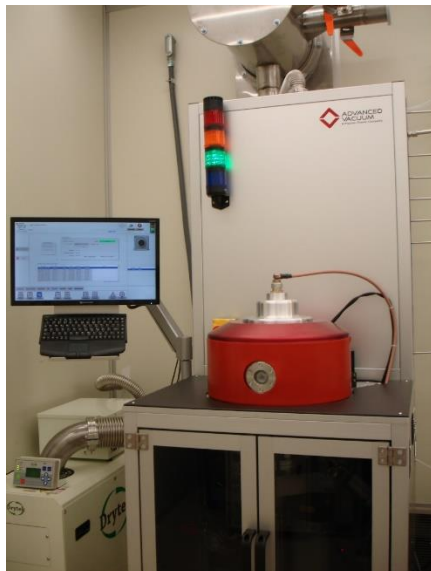


Figure A1.1 Plasma Therm plasma-enhanced chemical vapor deposition (PECVD) experimental setup.

#### A1.1 Loading sample:

1. See logbook and labrunner to check if the tool is UP.
  - a. Continue if there were no tool issues or tool issues have been addressed.
  - b. If tool issues have NOT been addressed, notify NaonoLab Staff.
2. Verify light tower is GREEN.
3. Check if Vision 310 Deck software and chamber is in operational condition.
  - a. The chamber and electrode are very hot.
  - b. Remove all foreign objects from the deck. If needed, use wipers or vacuum to remove any particles or debris.
4. Log into labrunner.
  - a. For existing reservation, start session.
  - b. Otherwise, make reservation and then start session.
5. Log into Vision 310 and type in the following:
  - a. User Name: Highlight USER
  - b. Password: Type in user
  - c. Click Log In

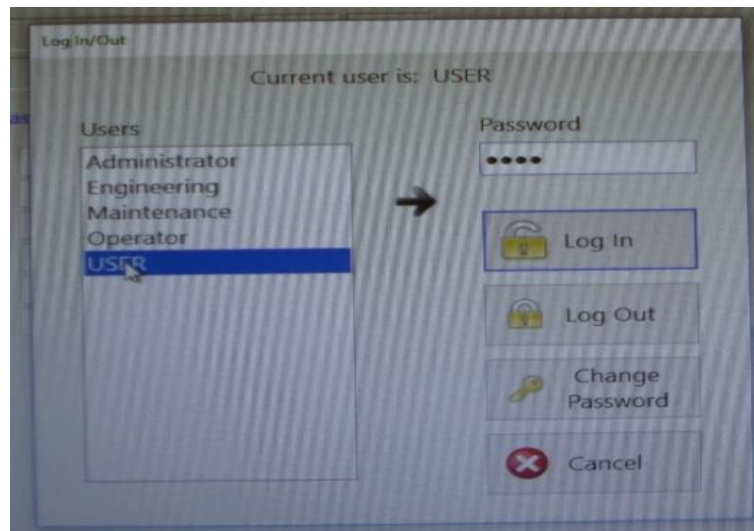


Figure A1.2 Plasma-enhanced chemical vapor deposition (PECVD) software login window.

6. Select appropriate recipe from menu.
  - a. If Chamber and/or Electrode temperature setpoints are not per process recipe, Click on Set Recipe Temps.
  - b. If chamber is at room temperature, wait until Chamber and Electrode meet setpoints.
  - c. When ready to load samples, continue.
7. To Vent Chamber, Click on Vent.
  - a. Wait until process status on right shows (PM1) 760 mT Vented.
8. To Open Lid, Click on Open Lid.
  - a. Prompt shows up to open the lid. Click yes to on Open Lid.
  - b. Stay clear of lid as it lifts up and swings to the right.
9. Load sample(s) in the center of stage
  - a. Do not touch stage with hands or fingers.
  - b. Do not drag cleanroom garment or wipers.
  - c. The stage is VERY HOT, severe burns may occur, and wipers or gloves can melt or catch fire.
10. To Close Lid, Click on Close Lid.
  - a. Prompt shows up to close the lid. Click yes to on Close Lid.
  - b. Stay clear of lid as it swings to the left and lowers.
  - c. If needed, wait until the Lid is fully lowered over the Electrode and has stopped moving. Then re-Open the lid.
11. To pump down Chamber, Click on Pump-down.
  - a. System begins pump-down sequence.
  - b. Wait for the Chamber pressure (PM1) to reach 0.3 mT.
12. Begin Logbook Entry.
  - a. Record requested data on the logbook.

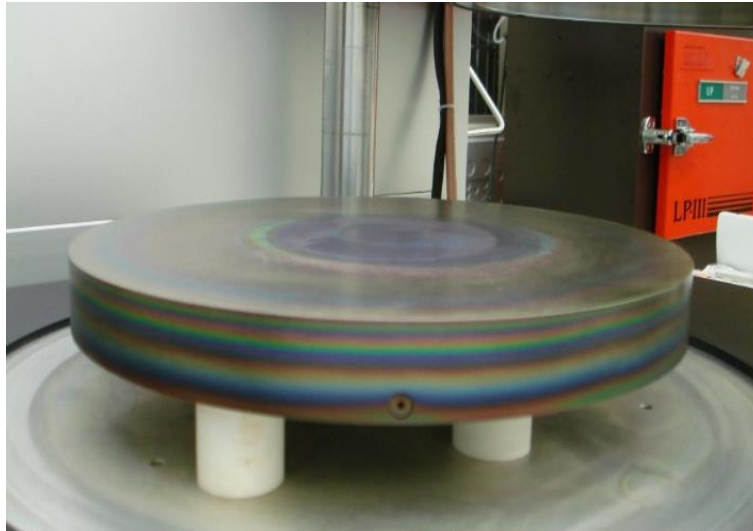


Figure A1.3 Plasma-enhanced chemical vapor deposition (PECVD) chamber stage and electrode.

## A1.2 Running recipe

### A1.2.1 Create Job ID:

1. Enter user defined Job Id. [Enter] in YYYYMMDD format.
2. Confirm appropriate recipe from menu.

### A1.2.2 Start Job:

1. Confirm that chamber and electrode are at setpoint temperatures.
2. Be sure a user defined Job Id has been entered in appropriate field.
3. When ready to start recipe, click on Start Job.
4. Enter Deposition Time.
5. Light tower turns BLUE.
6. Recipe has several required steps prior to deposition including an initialization step, temperature check and gas flow check (no plasma).
7. When recipe reaches deposition step, wait 1 minute for the tool to stabilize.
8. Record requested data on the logbook including any error, abort, alarm messages that occur during the run.
9. Wait for the tool to complete the recipe.

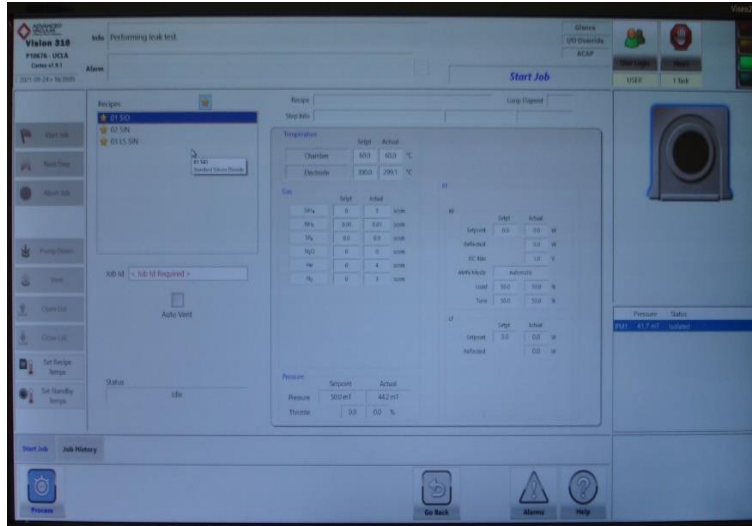


Figure A1.4 Plasma-enhanced chemical vapor deposition (PECVD) Vision 310 process window.

### A1.2.3 Unloading Sample

1. Confirm deck is clear of any obstacles.
2. To Vent Chamber, Click on Vent.
  - a. Wait until process status on right shows (PM1) 760 mT Vented.
3. To Open Lid, Click on Open Lid.
  - a. Prompt shows up to open the lid. Click yes to on Open Lid.
  - b. Stay clear of lid as it lifts up and swings to the right.
4. Unload sample with caution. Stage and electrode are very hot.
5. To Close Lid, Click on Close Lid.
  - a. Prompt shows up to close the lid. Click yes to on Close Lid.
  - d. Stay clear of lid as it swings to the left and lowers.
6. To pump down Chamber, Click on Pump-down.
  - a. System begins pump-down sequence.
  - b. Wait for the Chamber pressure (PM1) to reach 0.3 mT.
7. Complete Logbook Entry.

### A1.2 Plasma silicon dioxide (SiO<sub>2</sub>) and nitride (SiN) recipes:

Table A1.1 Silicon dioxide and nitride deposition recipes using silane, nitrous oxide, and ammonia.

Deposition	Recipe name in software	Deposition rate (Å/min)	Stress and Thickness (mPa)
Silicon dioxide	01 SiO	370	- 150 Compressive For Thickness 1000A
Silicon nitride	02 SiN	70	+ 275 Tensile For Thickness 1000A



### A1.3 Handling pellet in exhaust line:

#### A1.3.1 PPE:

1. Cleanroom gears (gown, goggles, hair net, shoe covers, gloves)
2. Face shield

#### A1.3.2 Safety hazard:

1. Immediately call EH&S and 911 upon contact and seek medical attention.

#### A2.7.3 Operating procedures:

1. Log in the labrunner and fill in the logbook.
2. Make sure:
  - a. All lid is CLOSED and chamber in PUMPDOWN
  - b. Pressure is  $< 1$  mT.
  - c. Clear Vision 310 Deck
  - d. If needed, use wipers or vacuum to remove any particles or debris.
  - e. Notify NanoLab Staff immediately if there are any problems or issues.
  - f. Be sure to record any problem or issue in the logbook.
  - g. To ensure safety, give 30 minutes of idle pumping after deposition.
  - h. Wear proper attire and PPE.
3. Close both valves of the tee to isolate the exhaust and open the capped end.
4. Extract the mesh carrier and put the cap back on.
5. Once the cap is sealed, open valve on the tee.

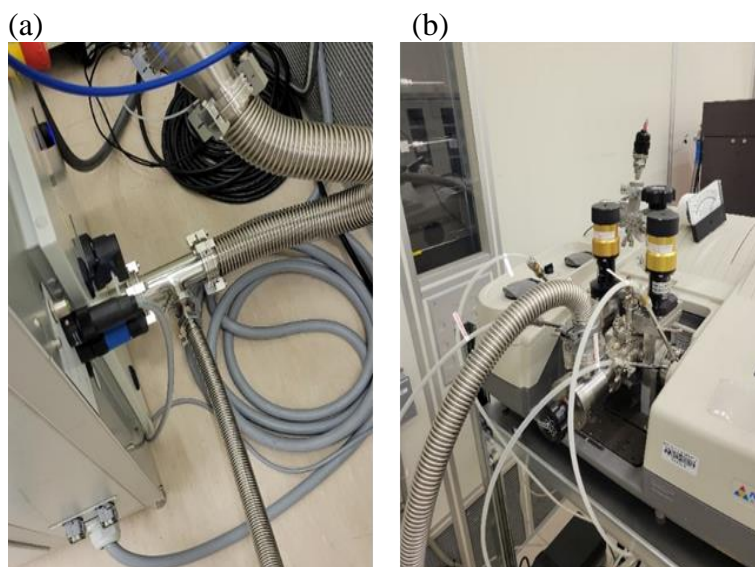


Figure A1.5 (a) Plasma-enhanced chemical vapor deposition (PECVD) exhaust extraction adaptor (ISO-K 63 tee) connection with (b) modified *in-situ* Nexus 670 Fourier transform infrared (FTIR) spectrometer in CNSI cleanroom.

## A2. Atomic layer deposition (ALD) standard operation procedures

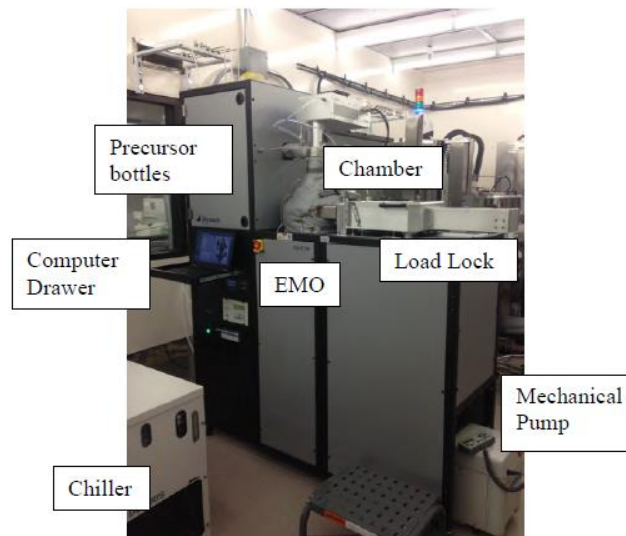


Figure A2.1 FIJI atomic layer deposition tool experimental setup (adapted from Y.-S Lin, 2017)

### A2.1 Emergency shutdown

1. Close all the precursor valves.
2. Press emergency off (EMO) button.
3. In system software press Program STOP button to turn off all outputs.
4. Head out to emergency exist a

### A2.2 Loading sample:

1. Log into Labrunner to disable the interlock.
2. Check the logbook to make sure previous runs were OK.
3. Check the Water Chiller:
  - a. Power is on (LED light appears green).
  - b. Temperature is below 70F.
  - c. Water flow is on.
4. Check the mechanical pump and make sure it is ok (POWER O" and RUNNING green lights are on).
5. Start filling out the logbook.
6. Make sure all the precursor valves are completely closed, if not, please report
  - a. From the Vacuum System tab, press LL VENT to vent the load lock chamber.
  - b. Wait 3 to 5 minutes until the load lock is completely vented. (Check the gap at load lock door).
7. Once the chamber is completely vented, Press OK on the software popup screen to turn off the load lock vent valve.
8. Lift the load lock door up when atmospheric pressure is reached.
9. Load wafer. Use the step stool to help reach the load lock door. Close the door down.
10. After loading your sample, close the door down.
11. From the Vacuum System screen, select Transfer Sample. Follow the system prompts. (The system automatically pumps down the load lock. After the pressure in the load lock and the process chamber is equilibrated, the main gate valve separating the two chambers

automatically opens; the substrate carrier is then loaded onto the heated chuck in the process chamber.)

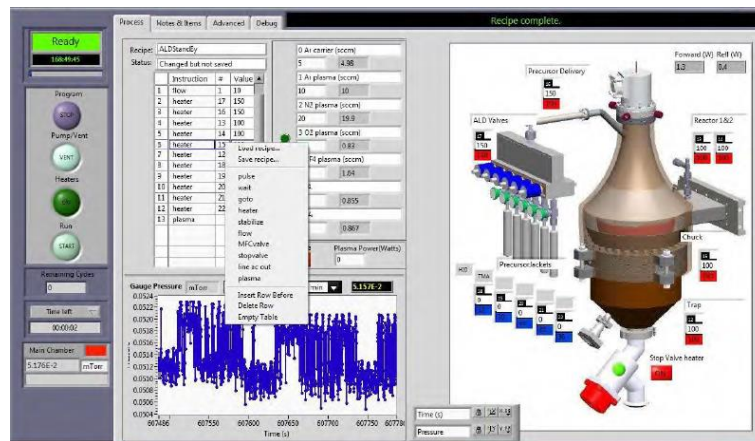


Figure A2.2 FIJI atomic layer deposition (ALD) operating software window (Cambridge NanoTech Inc., 2009).

#### A2.4 Loading and running recipe:

1. Go to Process Window and make sure that the system is pumped down.
2. Right click in the recipe steps table. Select the proper processing conditions from options menu.
  - a. Select the number of cycles at GOTO step.
  - b. Heater temperature (#12, #13, #14, #15) Typically at 200°.
  - c. Precursor Delivery line (#16 at 150°C) and precursor manifold (#17 at 150°C).
  - d. Precursor bottle temperature (TMA#18 and Zn#20 at room temperature set at 0. Hf #19, Ti #21 and Zr #22 at 75°C).
  - e. Set APC at 9% .
3. Do not overwrite the standard recipe. Ask nanolab staff for creation of new recipe.
4. Wait 10 minutes for the substrate/chamber to stabilize the temperature.
5. Open the appropriate precursor valve.
6. Press Start to run the recipe.
  7. Click Yes in the recipe start confirmation window.
  8. Record processing temperature and observe pulse time/process pressure.
  9. Once complete, close precursor valve.

#### A2.5 Unloading sample:

1. From the Vacuum System screen, select Transfer Sample. The substrate carrier should be automatically transferred to the Load Lock.
2. Wait for your substrate to cool to near room temperature (at least 20 minutes).
3. Go to Vacuum System screen, press LL Vent (approx. 2-3 minutes to vent). The load lock pressure should rise to 760 Torr and a dialogue box appears requesting acknowledgement that the LL is at atmospheric pressure. **DO NOT** acknowledge yet.
  - a. Gently try to lift the LL door. If it does not lift easily, wait another minute and try again. Repeat until it lifts easily.
  - b. Once the LL door can be opened easily, press OK in the dialogue box to acknowledge that the LL is at atmospheric pressure.
4. Fully open the LL door and remove wafer from the substrate carrier.
5. Close the LL door.
6. From the Vacuum System screen, select PumpChamber & LL without Turbo in order to

pump down both the chamber and load lock.

#### A2.6 Purging and cleaning system:

1. Make sure all precursor valves are close.
2. Go to Process Window and right click in the recipe steps table.
3. Select Al\_Headpurge or other headpurge recipe depending on which precursor you used.
4. Make sure both Door Purge and Main Turbo Purge are on by clicking on them
5. Press Start to run recipe.
6. After your run is completed, make sure the following settings are as follows:
  - a. Heater temperature setting
  - b. All precursor bottle temperature = 0°C
  - c. Heater Temperature (#12, #13, #14, #15) = 200°C
  - d. Precursor Delivery line (#16 at 150°C)
  - e. Precursor manifold (#17 at 150°C)
  - f. MFC0 Ar Carrier = 5 sccm
  - g. MFC1 Ar Plasma = 10 sccm
7. Turn off all 2 purges (dark green on the Vacuum System screen).
  - a. Door Purge
  - b. Main Turbo Purge
8. Fill in the logbook.

#### A2.7 Handling pellet in exhaust line:

##### A2.7.1 PPE:

1. Cleanroom gears (gown, goggles, hair net, shoe covers, gloves)
2. Face shield

##### A2.7.2 Safety hazard:

1. TMA is pyrophoric with a flash point of -4°C (24 F). The precursor is flammable, corrosive, irritant, toxic, and reacts violently with water.
2. Immediately call EH&S and 911 upon contact and seek medical attention.

##### A2.7.3 Operating procedures:

1. Log in the labrunner and fill in the logbook.
2. Make sure all the cleaning ALD valve via purge is completed and precursor valves are closed.
  - a. To ensure safety, give 30 minutes of idle pumping after deposition.
  - b. Wear proper attire and PPE
3. Close both valves of the tee to isolate the exhaust and open the capped end.
4. Extract the mesh carrier and put the cap back on.
5. Once the cap is sealed, open valve on the tee.

(a)

(b)

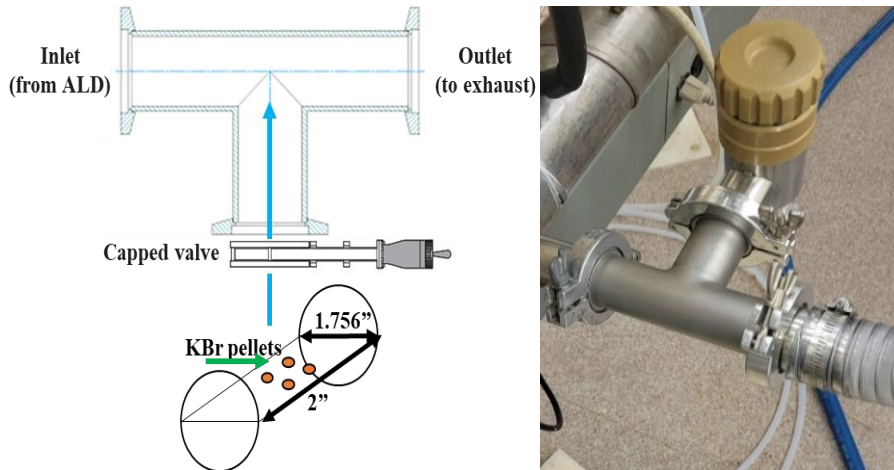


Figure A2.3 (a) Extraction unit implemented in the downstream area of atomic layer deposition (ALD) tool. (b) ALD exhaust extraction unit connection in EIV cleanroom

### A2.8 Thermal aluminum oxide ( $\text{Al}_2\text{O}_3$ ) recipe:

Table A2.1 Aluminum oxide deposition recipes using cycles of trimethyl aluminum (TMA) and  $\text{H}_2\text{O}$ .

Temperature ( $^{\circ}\text{C}$ )	TMA pulse (s)	TMA purge (s)	$\text{H}_2\text{O}$ pulse (s)	$\text{H}_2\text{O}$ purge (s)
300	0.06	5	0.06	5
250	0.06	8	0.06	8
200	0.06	10	0.06	10
150	0.06	20	0.06	20
100	0.06	30	0.06	30
75	0.06	60	0.06	60
50	0.06	120	0.06	120
25	0.06	180	0.06	180

Door purge = 50sccm

0.06s room temperature TMA pulse  $\approx 1.2\text{mg}$

### A2.8 Thermal hafnium oxide ( $\text{HfO}_2$ ) recipe:

Table. Hafnium oxide deposition recipes using cycles of tetrakis (dimethylamido) hafnium ( $\text{Hf}(\text{NMe}_2)_4$ ) and  $\text{H}_2\text{O}$ .

Temperature	$\text{Hf}(\text{NMe}_2)_4$ pulse	$\text{Hf}(\text{NMe}_2)_4$ purge	$\text{H}_2\text{O}$ pulse	$\text{H}_2\text{O}$ purge (s)
-------------	-----------------------------------	-----------------------------------	----------------------------	-----------------------------------

---

(°C)	(s)	(s)	(s)	
200	0.25	15	0.06	15
90	0.25	120	0.06	120

---

### A3. Potassium bromide (KBr) pellet preparation

#### A3.1 : Materials used:

1. Purchase KBr powder from International Crystal Laboratories (# 0011-8966)
2. Premium Grade FTIR SpectroGrade™ KBr Powder, 100 grams
3. CAS number: 7758-02-03
4. 100 mL Pyrex glass beaker (EV 1011)
5. Mortar and pestle (EV 1011)
6. Hydraulic press (YH 1043)
7. 13 mm Diameter pellet die set (YH 1043)
8. Desiccator (EV 1011 and CNSI cleanroom)
9. Mass balance (YH 1043 and 4505 MSB – Sletten Lab)

#### A3.2 PPE:

1. Gloves
2. Goggles for handling KBr powder
3. Mask for handling KBr powder

#### A3.3 Safety hazards:

1. KBr powder is irritant (Category 2A) and reproductive toxicity (Category 2)
2. Mechanical hazards while handling die set and hydraulic press.

#### A3.3 First-Aid:

1. Get medical attention if exposed.
2. If KBr eye contact, rinse and flush eyes thoroughly for at least 15 min
3. If KBr inhaled, move victim to fresh air and keep at rest in a position comfortable for breathing. If not breathing, if breathing is irregular or if respiratory arrest occurs, provide artificial respiration or oxygen by trained personnel.
4. If KBr ingested and the exposed person is conscious, give small quantities of water to drink. Stop if the exposed person feels sick as vomiting may be dangerous. Do not induce vomiting unless directed to do so by medical personnel. Remove dentures if any.
5. If KBr skin contact, rinse thoroughly for at least 15 min

#### A3.4 Pellet press procedure (refer to die set Figure 2.4):

1. Clean the spatula, tweezers, mortar, pestle, and the pellet die set with DI, acetone, and IPA.
2. Place 140 mg of KBr powder on a weighing boat with a spatula inside the mass balance
3. Use mortar and pestle to finely grind the weighed powder.
4. Configure the die set to before hydraulic press:
  - a. Place die base (1) on the bottom
  - b. Place die body (2) on top of the die base (1)
  - c. Insert die pellet (3) into the die body (2)
  - d. Use spatula to relocate powder in the mortar to top of the die pellet (3) inside die body (2)
  - e. Insert second die pellet (3) into the die body (2)
  - f. Plunger (4) is placed inside the die body (2) on top of the second die pellet (3)
5. With the die set configuration, place the set in the middle of the hydraulic press and press it with 10,000 lb for 3 minutes.
  - a. Pressure relief valve is located at the bottom of the hydraulic press.



Figure A3.1 Hydraulic press in YH 1043 with maximum pressure limit of 10,000 lb

6. Remove the pressed pellet from the die set configuration.
7. Slowly release the pressure of the hydraulic press to 0 lb and take out die set configuration from the press.
  - a. Remove the die base (1)
  - b. Place the die set configuration upside-down with plunger (4) contacting a flat surface.
  - c. Place an extraction ring on top of the die body (2), opposite of plunger (4)
  - d. Manually apply light load on the extractor ring until the pellet (3) and sample (6) are free from the die body (2)
8. Gently remove the sample KBr pellet with tweezers
9. Engrave one side of the pellet with a blade to indicate a side of the pellet that faces the exhaust of a deposition tool.
10. Weigh the pellet with microbalance.



#### A4. Fourier transform infrared (FTIR) spectroscopy standard operating procedure.

##### A4.1 Preparing tool for operation

###### A4.1.1 Purging the FTIR:

1. Start to purge FTIR by dry N<sub>2</sub> (start with 35 psi).
  - a. clockwise turn “1” to about ~35 psi
  - b. Open green handle “2”
  - c. turn to “off” for pressure release valve “3”
  - d. Open green handle “4” to provide N<sub>2</sub> gas to regulator



Figure A4.1 FTIR N<sub>2</sub> purge gas and liquid N<sub>2</sub> tank configuration (adapted from Z. Loh, 2010).

###### A4.1.2 Detector cooldown:

1. Cool down the detector (InSb, MCT\_HD) by using liquid N<sub>2</sub> (wait ~30 for best detecting S/N ratio).
2. Check or switch the beam splitter (Quartz, KBr, CaF<sub>2</sub>)

##### A4.2 Software operation

###### A4.2.1 Bench setup:

1. In OMNIC software, open Experiment Setup window and navigate to Bench tab, select the following parameters:
  - a. Sample compartment: main
  - b. Detector: InSb or MCT\_HD
  - c. Beam Splitter: CaF<sub>2</sub>, KBr, or Quartz
  - d. Source: White light source
  - e. Gain: 1.
  - f. Aperture: 5
  - g. Screen wheel: 2%
2. Wait 10-15 minutes for white light power to stabilize.

###### A4.2.2 Alignment setup:

3. In OMNIC software, open Experiment Setup and navigate to Diagnostic tab. Run Internal Alignment (Peak to Peak should be in range of 0.7– 3.0).
4. Wait for 1-2 minutes to finish the self-alignment.

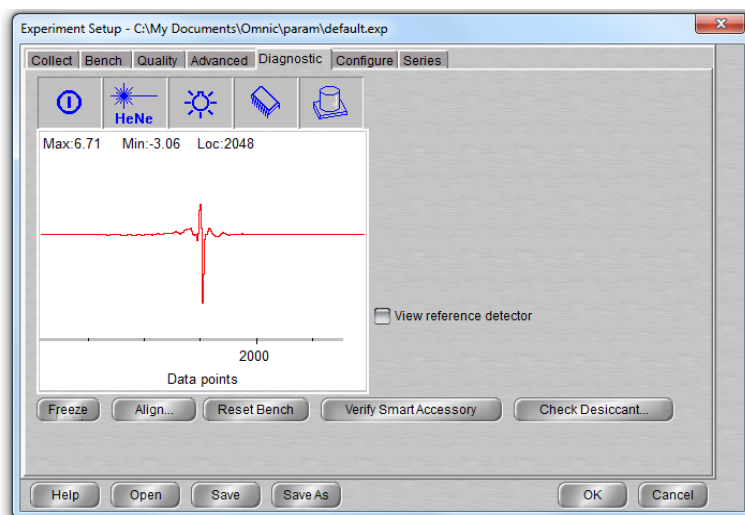


Figure A4.2 OMNIC software Experiment Setup window with Diagnostic tab.

#### A4.2.2 Collection setup:

1. In OMNIC software, open Experiment Setup window and navigate to Bench tab, select the change the following:
  - a. Source: IR
  - b. Max – min range limit: 4000 – 400
  - c. Gain: 4.0
  - d. Aperture: 10
  - e. Screen wheel: 10% (change to 20% or open once sample is in)

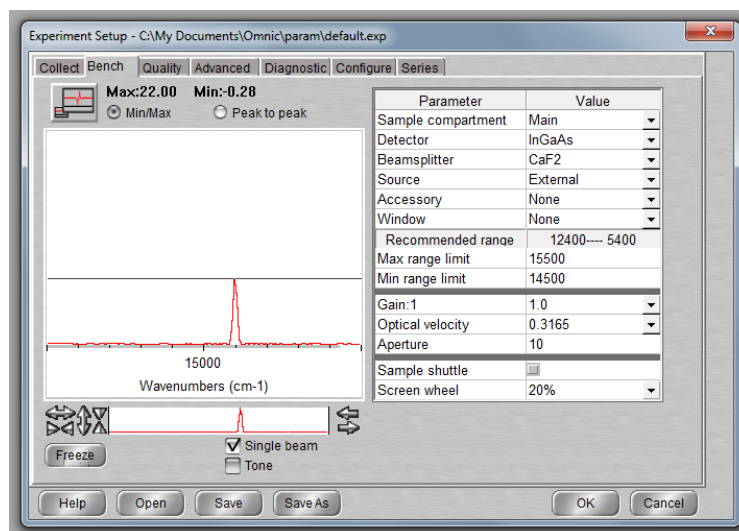


Figure A4.2 OMNIC software Experiment Setup window with Bench tab.

2. In OMNIC software, open Experiment Setup window and navigate to Collection tab, select the following parameters:
  - a. No. of Scans: 128
  - b. Resolution: 4
  - c. Final Format: % Transmittance or Absorption
  - d. Correction: None

- e. Collect background before every sample

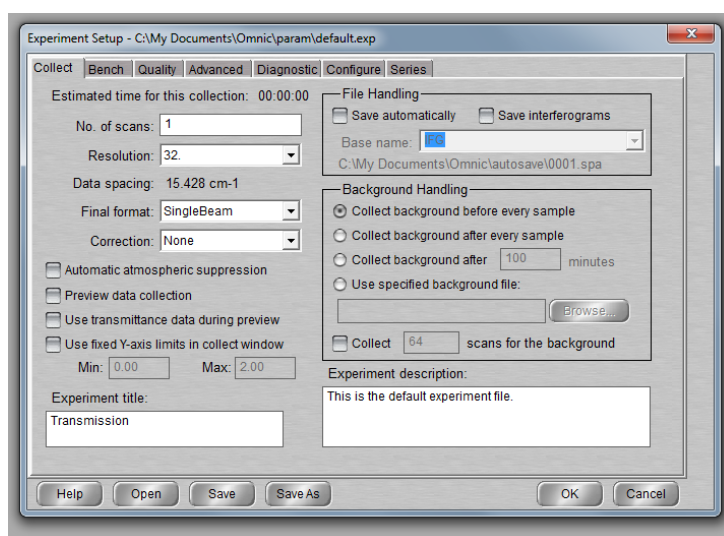


Figure A4.3 OMNIC software Experiment Setup window with Collect tab.

#### A4.2.3 Data collection:

1. In OMNIC software press Col BKG for reference background collection
2. Press Col SMP for IR data collection (depending on Collect setup, background can be taken before/after every sample)
3. Once data collection is complete, navigate to Display setup to change axis value, range, and information.
  - a. Data can be subtracted from one another to remove signals from one or the other
4. Save the data file by pressing F12 in CSV, txt, or SPA format.
5. Once data collection is completed, navigate to Experiment Setup window and Bench tab to select parameters and turn source off.

## A5. X-ray photoemission spectroscopy (XPS) standard operation procedure

### A5.1 PPE:

1. Gloves
2. Goggles



Figure A5.1 Kratos DLD Axis Ultra XPS ver2.0 (adapted from I. Martini, 2014).

### A5.2 Startup conditions:

1. Reserve instrument if available and sign in on the logbook.
2. Instrument Vision Manager (Manager, Manual, Processing and Sys Administrator) should be open and have Controller Processor Unit in the instrument display d3.
  - a. If software is not open Zones application and hit OK on the error message.
  - b. On the Zone taskbar, click Shortcut to Manager and click on Window menu.
  - c. Open Instrumental Manual Control window and Real time display
  - d. Navigate to Control tab and drag the manual and real time display windows into the manual zone.
  - e. Calibrate the stage by calibrate axes and calibrate request from the parameters section of Instrument Manual Control window.
3. Click on the Manual zone in the top task bar and open Instrument Manual Control window.
4. Check SAC conditions as following:
  - a. SAC pressure:  $< 1 \times 10^{-8}$
  - b. STC (or SEC) pressure:  $< 5 \times 10^{-7}$
  - c. Vacuum Control Unit: display standby condition or Instrument Manual Control window (Figure A5.2).
  - d. If any deviation is noted, notify staff and do not proceed.

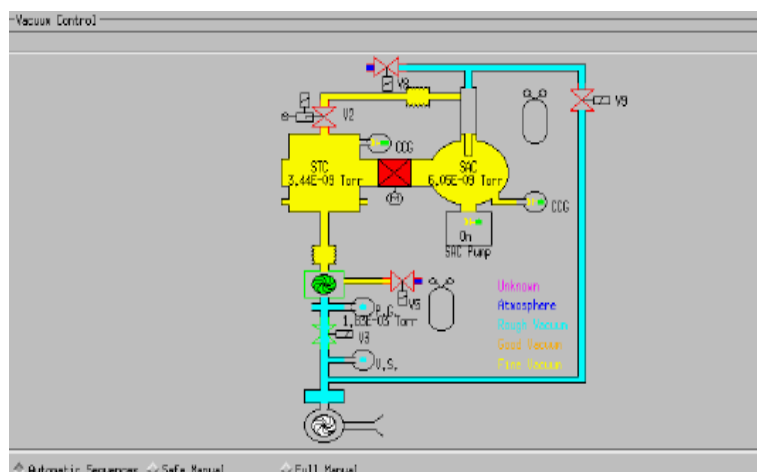


Figure A5.2 Vacuum meters for both STC and SAC chambers from Instrument Manual Control window (adapted from I. Martini, 2014).

### A5.3 Loading and unloading samples to sample transfer chamber (STC):

1. On the sample Stub attach your samples
2. Click on Instrument Manual Control window to Manual tab then to Vacuum Control section.
3. Click Automatic Sequence to see green light at the tip of transfer arm barrel not red.
4. Click Vent STC
5. Vent for approximately 2 minutes after partially loosening three brass screws of the STC chamber.
6. On Vacuum Control Unit, click Advance to stop nitrogen purge.
7. Completely loosen brass screws and open STC chamber door
8. Move transfer arm forward and load sample on a Stub by rotating transitional knob.
9. Attach the sample Stub to the transfer arm.
10. Rotate knob and move the transfer arm so that the sample stub does not collide with the chamber opening when closing the chamber door.
11. Close the chamber door and partially tighten the brass screws.
12. Move the transfer arm forward by rotating the knob and rotate the wheel underneath the STC to switch a Stub position on the way of the transfer arm.
13. Rotate the wheel once the Stub reached the end position to release the Stub from the transfer arm.
14. Rotate the transfer arm back until the green light on window shows up,
15. Click Pump and hold the door of STC chamber for initial pump down.
16. Tightly screw the brass screw on the STC chamber door and let it pump down for approximately 15 minutes.
17. Check for Automatic Sequence Successfully Complete notification on Vacuum Control Section window.
18. Check for pressure before leaving.

### A5.4 Loading samples to sample analysis chamber (SAC) (DO NOT open if chamber pressure $> 5 \times 10^{-7}$ ; confirm with EMAL staff before performing this step):

1. Check if Bar or Stub is loaded and refer to A5.5 if you need to unload.
2. In the Instrument Manual Control window, click Manual tab then Vacuum Control section.
3. Check for green light (not red) at the end of transfer arm after clicking on Automatic Sequence.

4. Open STC-SAC valve and wait for valve open notification.
5. Verify the Dual Anode X-ray source is backed out from the sample area.
6. Click on Position in Manipulator section in the Instrument Manual Control window.

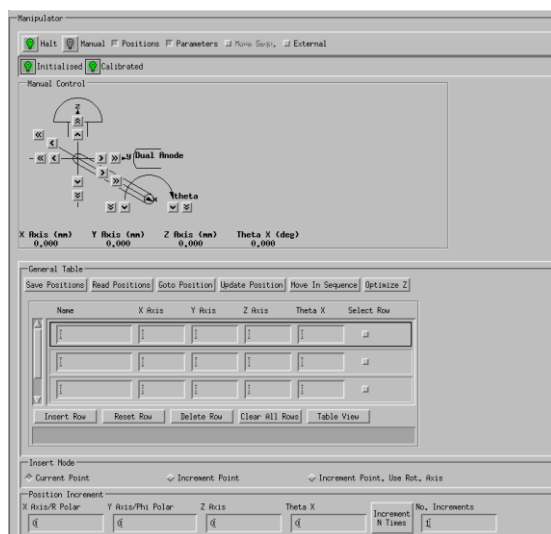


Figure A5.3 Manipulator section from Instrument Manual Control window (adapted from I. Martini, 2014).

7. Click on Go to Position to move the stage for transferring the sample holder.
  - a. If Load Bar or Load\_Stub positions are not displayed in the position table rows click on Read Positions.
  - b. Choose loadbar.dset or load\_stub.dset.
8. In Manipulator window click on Manual
9. Look at the window and rotate the translation knob to move the sample into the SAC chamber for the interlinks with stage and stops.
10. Use Autostage Manual Controller and move stage away from the transfer arm, releasing the sample holder from the arm.



Figure A5.4 Autostage Manual Controller.

11. Rotate the knob and remove arm from SAC chamber until green light is shown.
12. Under Vacuum Control section click on STC-SAC Valve in the Instrument Manual Control.
13. Position the sample using the Autostage Manual Controller while observing the video

monitor.

A5.5 Unloading samples from sample analysis chamber (SAC) (DO NOT open if chamber pressure  $> 5 \times 10^{-7}$ ; confirm with EMAL staff before performing this step):

1. In the Instrument Manual Control window click Manipulator section then Position.
2. Click on Read Position then choose Unloadbar or Unloadstub.
3. Move the stage to the position for transferring sample holder by clicking Go to Position.
4. Click Manual in the Manipulator section.
5. In Automatic Sequence window, click Open STC-SAC Valve.
6. Rotate the translation knob to move the sample holder into the SAC chamber until it interlinks with the stage and stops while looking at the window.
7. Use Autostage Manual Controller and move stage toward the transfer arm, releasing the sample holder from the stage.
8. Rotate the knob and move transfer arm away from SAC chamber until the green light is shown.
9. Click on Close STC-SAC Valve and have valve closed.

A5.6 Performing survey scans

1. From Vision Instrument Manager window, click on Manager.
2. Click Resume and set Automatic mode.
3. To save click Dataset button.
4. Click Acquisition and set parameters as following for the scan:
  - a. Name: Survey
  - b. Standby control: Leave On (leaves X-rays on after scan completed)
  - c. Analyzer mode: Spectrum
  - d. Analyzer lens mode: Hybrid
  - e. Analyzer resolution: Pass Energy 160
  - f. Analyzer aperture: Slot (700 x 300  $\mu\text{m}$ )
  - g. Number of detectors: 115
  - h. Charge neutralizer: Under Manual Control
  - i. Scan control region name: Survey
  - j. Scan control start eV: 1200
  - k. Scan control end eV: -5
  - l. Scan control dwell ms: 200
  - m. Scan control 3 sweeps: 1
  - n. Click on Active
5. Paste Survey in the sequence flow chart.
6. Click Submit to start the flow chart.
7. Click Acquiring in the Real-Time Display window. The Viewing Acquiring Session window turns pink during data collection and grey when finished.
8. After completion, the Real-Time Display window shows the scan. Control menus can help changing parameters of the scans.
  - a. From the Windows pull down menu choose element of interest to identify peaks.

A5.7 Performing region scans:

1. In Vision Instrument Manger window click on Manger. In the flow chart name your scan.
2. Set up Acquisition parameters for scan at Scan Control section.
  - a. Charge balance: 2.6 – 3.2 V
  - b. Filament current: 1.6 – 2.1 A
  - c. Filament bias: 0.9 – 1.3 V

d. Large area (300um x 700 μm) – slot\_

Energy range	Magnification	Pass energy (eV)	Step size (eV)	Time (mins)
Survey	hybrid	160	1	1 - 3
Region	hybrid	10 or 20	0.1	1 - 10
Valence Band	hybrid	20 or 40	0.2	5 - 20

3. From Manager window, use pull down Windows menu to select Scan Control.
4. In the Real-Time Display window, click on the peak of interest and associated element from the list.
5. Enter region of interest manually and settings are loaded automatically.
6. Hit Active to scan.
7. Once completed, click Submit to start the flowchart. Acquiring in view window can display data being collected.
8. Once completed, save data.
9. Open dset using Vision Processing then open Browser Action window.
10. From Describe tab, click Destination and convert to Vamas File then apply.
  - a. CASA XPS is able to open .vms file.

A5.8 Standby mode:

1. Do not close or exit any windows or software.
2. First click Standby then Off to turn off X-ray source.
3. Set Emission to 1 and HT to 6 in the X-ray PSU.
4. In Vision Manager window, clear flowcharts and choose Close Dataset in acquisition.
5. In Process window, choose Close all Datasets and Clear Scratch from File tab.
6. Open Manual Control Window from Manual tab.
7. Turn off monitor and complete logbook.



## Bibliography

- Alda, M., Mega, Y., Mizuno, K., Biagi, L., & Dulin, C. (2023). Semiconductors - worldwide: Statista market forecast. Semiconductors - Worldwide.
- Allendorf, M. D., Melius, C. F., Cosic, B., & Fontijn, A. (2002). BAC-G2 predictions of thermochemistry for gas-phase aluminum compounds. The Journal of Physical Chemistry A, **106**(11), 2629–2640.
- Allendorf, M. D., Melius, C. F., Ho, P., & Zachariah, M. R. (1995). Theoretical study of the thermochemistry of molecules in the Si-O-H system. The Journal of Physical Chemistry, **99**(41), 15285–15293.
- Arai, M. (2000). Explosion of accumulated substances on opening of exhaust piping at a semiconductor manufacturing factory. Failure Knowledge Database.
- Barreca, D., Milanov, A., Fischer, R. A., Devi, A., & Tondello, E. (2007). Hafnium oxide thin film grown by ALD: An XPS study. Surface Science Spectra, **14**(1), 34–40.
- Biesinger, M. (2021). X-ray Photoelectron Spectroscopy (XPS) Spin Orbit Splitting. Canada, Ontario: Surface Science Western.
- Bolmen, R. A., Jr. (1989, July). Managing the integration of safety in semiconductor manufacturing. Solid State Technology, **32**(7), 63+.
- Burgess, D. R. F., Zachariah, M. R., Tsang, W., & Westmoreland, P. R. (1995). NIST Technical Note 1412. In Thermochemical and chemical kinetic data for fluorinated hydrocarbons. Washington, MA: National institute of standards and technology.
- Cambridge NanoTech Inc. (2009). FIJI F200 Atomic Layer Deposition System Installation and Use Manual, 2(01). ts, Cambridge.
- Chambers, A. (2016). Managing hazardous process exhausts in high volume manufacturing. Solid State Technology.
- Chang, Y.-H., Kishore, J., & Shadman, F. (2019). Run-away energetic reactions in the exhaust of deposition reactors. Advances in Chemical Engineering and Science, **09**(02), 223–238.
- Chemplex ®. (2019). Evacuatable pressing die set & pellet for XRF. Chemplex Industries, Inc.
- Cho, J. L. (2015). Engineering lithium ion conducting thin film solid electrolytes by atomic layer deposition. University of California, Los Angeles, Los Angeles.
- Choudhury, S., Kumar, A., & Kumar, N. (2021). Silane: Risk Assessment, environmental, and Health Hazard. Hazardous Gases, 353–362.

- Ciurczak, E. W., Igne, B., Workman, J., & Burns, D. A. (2021). Handbook of Near-Infrared Analysis. Boca Raton, FL, NY: CRC Press, Taylor & Francis Group.
- Goldstein, D. N., McCormick, J. A., & George, S. M. (2008). Al<sub>2</sub>O<sub>3</sub> Atomic Layer Deposition with Trimethylaluminum and Ozone Studied by in Situ Transmission FTIR Spectroscopy and Quadrupole Mass Spectrometry. The Journal of Physical Chemistry, **112**(49), 19530–19539.
- Han, S. M., & Aydil, E. S. (1996). Study of surface reactions during plasma enhanced chemical vapor deposition of SiO<sub>2</sub> from SiH<sub>4</sub>, O<sub>2</sub>, and Ar Plasma. Journal of Vacuum Science & Technology A: Vacuum, Surfaces, and Films, **14**(4), 2062–2070.
- Harris, D. C., & Bertolucci, M. D. (1989). Symmetry and spectroscopy. Mineola, NY: Dover Publications, Inc.
- Hirano, T. (2002). Accidental explosions of semiconductor manufacturing gases in Japan. Journal de Physique IV (Proceedings), **12**(7), 253–258.
- Ho, M.-T., Wang, Y., Brewer, R. T., Wielunski, L. S., Chabal, Y. J., Moumen, N., & Boleslawski, M. (2005). *in situ* infrared spectroscopy of hafnium oxide growth on hydrogen-terminated silicon surfaces by atomic layer deposition. Applied Physics Letters, **87**(13).
- Hofstetter, Y. J., & Vaynzof, Y. (2019). Quantifying the damage induced by X-ray photoelectron spectroscopy depth profiling of organic conjugated polymers. ACS Applied Polymer Materials, **1**(6), 1372–1381.
- Jaszewski, S. T., Calderon, S., Shrestha, B., Fields, S. S., Samanta, A., Vega, F. J., Minyard, J. D., Casmento, J. A., Maria, J.-P., Podraza, N. J., Dickey, E. C., Rappe, A. M., Beechem, T. E., Ihlefeld, J. F. (2023). Infrared signatures for phase identification in hafnium oxide thin films. ACS Nano, 23944-23954
- Kim, K. C., Allendorf, M. D., Stavila, V., & Sholl, D. S. (2010). Predicting impurity gases and phases during hydrogen evolution from complex metal hydrides using free energy minimization enabled by first-principles calculations. Physical Chemistry Chemical Physics, **12**(33), 9918.
- Larkin, P. (2011). IR and Raman Spectroscopy: Principles and spectral interpretation. Oxford, MA: Elsevier.
- Lin, Y.-S. (2017). FIJI Thermal and Plasma Atomic Layer Deposition System (ALD) By Ultratech (Cambridge). ts, Los Angeles.
- Liu, Y., Lim, N., Smith, T., Sang, X., & Chang, J. P. (2021). Thermochemical prediction of runaway energetic reactions involving organometallic (Al, in) and silane precursors in deposition tools. Journal of Vacuum Science & Technology B, **40**(1).
- Loh, Z. (2010). FTIR Manual, PL, Calibration, Alignment. ts, Los Angeles.

- Ludwig, B., & Burke, T. T. (2022). Infrared spectroscopy studies of aluminum oxide and metallic aluminum powders, part I: Thermal dehydration and decomposition. Powders, **1**(1), 47–61.
- Martini, I. (2014). Operation Procedure for the DLD Axis Ultra XPS. ts, Los Angeles.
- Nakamoto, K. (2008). Infrared and Raman spectra of Inorganic and Coordination Compounds, **6**(1). Hoboken, NJ: Wiley.
- Nyquist, R. A., & Kagel, R. O. (1997). Infrared Spectra of Inorganic Compounds: (3800-45CM-1). San Diego, NY: Academic Press.
- Ogita, Y.-I., Iehara, S., & Tomita, T. (2003). Al<sub>2</sub>O<sub>3</sub> formation on Si by catalytic chemical vapor deposition. Thin Solid Films, **430**(1–2), 161–164.
- Pereyra, I., & Alayo, M. I. (1997). High quality low temperature DPECVD silicon dioxide. Journal of Non-Crystalline Solids, **212**(2–3), 225–231.
- SEMI (2020). SEMI S30 - Safety Guideline for Use of Energetic Materials in Semiconductor R&D and Manufacturing Processes. ms, Milpitas.
- Seo, S., & Song, Y.-W. (2021). A study on the safe hydrogen exhaust method in the semiconductor industry. Asia-Pacific Journal of Convergent Research Interchange, **7**(6), 1–10.
- Settle, F. A. (1997). Handbook of Instrumental Techniques for Analytical Chemistry. Upper Saddle River, NJ: Prentice Hall PTR.
- Skulan, A. J., Nielsen, I. M., Melius, C. F., & Allendorf, M. D. (2005). BAC-MP4 predictions of thermochemistry for gas-phase indium compounds in the In–H–C–O–Cl system. The Journal of Physical Chemistry A, **110**(1), 281–290.
- Sperling, B. A., Kalanyan, B., & Maslar, J. E. (2020). Atomic Layer Deposition of Al<sub>2</sub>O<sub>3</sub> Using Trimethylaluminum and H<sub>2</sub>O: The Kinetics of the H<sub>2</sub>O Half-Cycle. The Journal of Physical Chemistry C, **124**(5), 3410–3420.
- Stuart, B. H. (2005). Infrared Spectroscopy: Fundamentals and Applications. Chichester(Royaume Uni): J. Wiley & Sons.
- Tokunaga, L. (2022). Plasma Therm Vision 310 Operation. ts, Los Angeles.
- Trammell, S. (2014). SESH A 36th Annual Symposium. In New Materials Introductions for Next Generation Semiconductor Manufacturing: ESH Challenges. Scottsdale, AZ: SESH A.
- Tsuda, K. (2014). Explosion at Mitsubishi Materials. Semiconductor Engineering.
- Wagner, C. D. (1983). Sensitivity factors for XPS analysis of surface atoms. Journal of Electron Spectroscopy and Related Phenomena, **32**(2), 99-102.

Wang, Y., Ho, M.-T., Goncharova, L. V., Wielunski, L. S., Rivillon-Amy, S., Chabal, Y. J., Moumen, N., Boleslawski, M. (2007). Characterization of ultra-thin hafnium oxide films grown on silicon by atomic layer deposition using tetrakis(ethylmethyl-amino) hafnium and water precursors. Chemistry of Materials, **19**(13), 3127–3138.

Watson, E., & Shadman, F. (2020). Preventing hot-spot formation in the exhaust system of deposition reactors. International Journal of Emerging Technology and Advanced Engineering, **10**(2), 62-68.

Zarchi, M., Ahangarani, S., & Sanjari, M. Z. (2014). Properties of silicon dioxide film deposited by PECVD at low temperature/pressure. Metallurgical and Materials Engineering, **20**(2), 89–96.